INTERPRETING SATELLITE REMOTE SENSING OBSERVATIONS USING A
CHEMICAL TRANSPORT MODEL: IMPLICATIONS FOR PROCESSES AFFECTING
TROPOSPHERIC NOX AND OZONE

by

Matthew J. Cooper

Submitted in partial fulfilment of the requirements
for the degree of Doctor of Philosophy

at

Dalhousie University
Halifax, Nova Scotia
August 2016

TABLE OF CONTENTS

List of Tables

List of Figures

Abstract

Nitrogen oxides (NO_x = NO + NO_2) and ozone (O_3) play important roles in the troposphere that impact air quality and climate. This thesis presents three projects that demonstrate how satellite observations interpreted with a chemical transport model can provide insight into emission, chemistry, and transport processes that affect NO_x and O_3 concentrations in the troposphere.

Satellite observations from three instruments (MLS, OSIRIS, ACE-FTS) are used to reveal coherent patterns of low ozone events (< 20 ppbv) in the tropical upper troposphere. Modeling studies using the GEOS-Chem chemical transport model indicate that these events result from deep convective processes that rapidly transport ozone-depleted air from the marine boundary layer. The satellite observations indicate spatial shifts in the frequency of low ozone events that arise from changes in convection associated with the El Niño and Madden-Julian Oscillations.

A comparison between nitric acid (HNO_3) columns from the IASI satellite instrument and those simulated with GEOS-Chem reveal a model underestimation over Southeast Asia. Sensitivity studies indicate that this bias is likely driven by nonlinear chemistry effects during the lightning NO_x parameterization. We tested a subgrid lightning plume parameterization and found that an ozone production efficiency of 15 mol/mol in lightning plumes over Southeast Asia with an additional 0.5 Tg N would reduce the regional nitric acid bias from 92% to 6%.

The GEOS-Chem adjoint model is used as a benchmark to evaluate mass balance methods for inverse modeling of NO_x emissions from synthetic NO_2 columns. We find that error in mass balance inversions can be reduced by a factor of two by using an iterative process that utilizes finite difference to linearize the model around its *a priori* state. The iterative finite difference mass balance and adjoint-based 4D-Var methods produce similar top-down inventories when inverting hourly synthetic observations, reducing the *a priori* error by a factor of 3-4. Inversions of synthetic satellite observations from low Earth and geostationary orbits also indicate that the finite difference mass balance and adjoint-based 4D-Var inversions produce similar results, reducing *a priori* error by a factor of 3.

List of Abbreviations and Symbols Used

Symbol	Units	Description
4D-Var		Four Dimensional Variational Data Assimilation
ACE-FTS		Atmospheric Chemistry Experiment Fourier Transform Spectrometer
CO		Carbon Monoxide
DOFS		Degrees of Freedom of Signal
ENSO		El Niño-Southern Oscillation
GC		GEOS-Chem Chemical Transport Model
GEOS		Goddard Earth Observing System
GMAO		Global Modeling and Assimilation Office
GOME2		Global Ozone Monitoring Experiment-2
HIRDLS		High Resolution Dynamics Limb Sounder
HNO_3		Nitric Acid
IASI		Infrared Atmospheric Sounding Interferometer
LEO		Low Earth Orbit
MJO		Madden-Julian Oscillation
MLS		Microwave Limb Sounder
NME	%	Normalized Mean Error
NO_x		Nitrogen Oxides
NO_y		Total Odd Nitrogen
O_3		Ozone
OLR	$W\ m^{-2}$	Outgoing Longwave Radiation
OMI		Ozone Monitoring Instrument
OPE		Ozone Production Efficiency
OSIRIS		Optical Spectrography and Infrared Imaging System
PAN		Peroxyactyl nitrate
PEM		Pacific Exploratory Mission
ppbv		Parts per billion by volume
r		Correlation Coefficient
SHADOZ		Southern Hemisphere Additional Ozonesondes
SST	K	Sea Surface Temperature
VOC		Volatile Organic Compound
β		Finite Difference Mass Balance Scaling Factor
γ_R		Cost function regularization parameter
σ		Standard Deviation
Ω	$molecules\ m^{-2}$	Column abundance

Acknowledgements

Chapter 1: Introduction

1.1 Tropospheric Nitrogen Oxide and Ozone

Nitrogen oxides (NO + NO_2 = NO_x) and ozone (O_3) are involved in a wide variety of processes in the troposphere, affecting air quality, atmospheric oxidation, and climate. Elevated concentrations of NO_2 contribute to poor surface air quality and are associated with increased mortality rates [*Burnett et al.*, 2004]. NO_2 can oxidize to produce aerosol nitrate particles that can affect climate through direct or indirect radiative forcing effects [*Adams et al,* 2001]. Alternatively, NO_2 oxidation can produce nitric acid (HNO_3) which can cause soil and groundwater acidification upon deposition [*Zhang et al.,* 2012]. NO_x is also a catalyst that enables the production of tropospheric ozone. Ozone is a precursor to the hydroxyl radical, and is therefore important to oxidation of trace gases in the troposphere [*Thompson,* 1992]. Near the surface, ozone is a contributor to poor air quality affecting human respiratory health and plant growth [*EPA,* 2014]. Ozone absorbs outgoing infrared radiation at 9.6 μm and therefore acts as a greenhouse gas in the upper troposphere, affecting the atmosphere's radiation budget [*Lacis et al.,* 1990]. A strong understanding of the physical and chemical mechanisms that impact tropospheric NO_x and O_3 is therefore essential for both health and climate related research.

The following sections present an overview of processes that influence NO_x and ozone concentrations in the troposphere.

1.1.1 NO_x Chemistry

Nitrogen oxides (NO and NO_2) are grouped as the collective family NO_x as they exist in a steady state due to rapid cycling:

$$NO + O_3 \rightarrow NO_2 + O_2 \tag{1 - 1}$$

$$NO_2 + h\upsilon \rightarrow NO + O_3 \tag{1 - 2}$$

The main sink of NO_x is oxidation of NO_2 forming HNO_3:

$$NO_2 + OH + M \rightarrow HNO_3 + M \qquad (1 \text{-} 3)$$
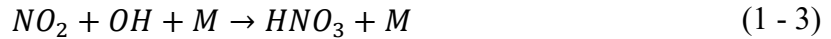
Since OH is produced photochemically, it is only present in the daytime. At night, NO_x is converted to N_2O_5 and then to HNO_3:

$$NO_2 + O_3 \rightarrow NO_3 + O_2 \qquad (1 \text{-} 4)$$

$$NO_3 + NO_2 + M \rightarrow N_2O_5 + M \qquad (1 \text{-} 5)$$

$$N_2O_5 + H_2O \rightarrow 2HNO_3 \qquad (1 \text{-} 6)$$

HNO_3 is highly soluble and is readily removed from the troposphere by wet deposition [*Mari et al.,* 2000].

The lifetime of NO_x in the troposphere is relatively short (approximately a day) and therefore NO_x is not transported over long distances. However, NO_x can be converted into longer-lived reservoir species that are able to be transported long distances. The most important reservoir species for NO_x is peroxyacetyl nitrate (PAN), which has a lifetime of several months at temperatures typically found in the middle and upper troposphere and is not easily deposited. PAN is easily transported long distances aloft, and then decomposes into NO_x following subsidence into warmer air.

1.1.2 Tropospheric Ozone Chemistry

Ozone production occurs in the troposphere during oxidation of carbon monoxide and volatile organic compounds in the presence of nitrogen oxides via the following reactions [*Crutzen,* 1979; *Lin et al.,* 1988]:

$$CO + OH \rightarrow H + CO_2 \qquad (1 \text{-} 7)$$

$$H + O_2 + M \rightarrow HO_2 + M \qquad (1 \text{-} 8)$$

$$HO_2 + NO \rightarrow OH + NO_2 \qquad (1 \text{-} 9)$$

$$NO_2 + h\upsilon \rightarrow NO + O \qquad (1 \text{-} 10)$$

$$O + O_2 + M \rightarrow O_3 + M \qquad (1 \text{-} 11)$$

$$Net: \quad CO + 2O_2 \rightarrow CO_2 + O_3 \qquad (1 \text{-} 12)$$
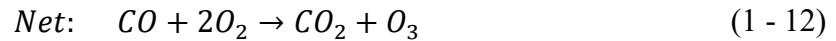
As NO_x acts as a catalyst in this process, a single NO_x molecule may be responsible for the production of multiple ozone molecules. NO_x is the rate limiting precursor to ozone production throughout most of the troposphere [*Jaeglé et al.,* 1998a], and thus proper evaluation of NO_x emissions is essential to understanding ozone production.

The main sink for tropospheric O_3 is photochemical, via:

$$O_3 + h\upsilon \rightarrow O_2 + O(\,^1D) \qquad (1 \text{-} 13)$$

$$O(\,^1D) + H_2O \rightarrow 2OH \qquad (1 \text{-} 14)$$
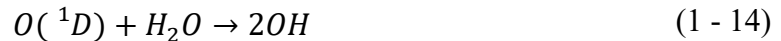
In remote regions with low NO_x concentrations, ozone loss can also occur via catalytic cycling of OH and HO_2:

$$O_3 + OH \rightarrow HO_2 + O_2 \qquad (1 \text{-} 15)$$

$$O_3 + HO_2 \rightarrow OH + 2O_2 \qquad (1 \text{-} 16)$$

These sinks restrict ozone concentrations to less than 20 ppbv throughout the lower troposphere, and as low as a few ppbv in the tropical marine boundary layer where humidity is high and solar radiation is intense [*Thompson*, 1992; *Kley et al.*, 1996]. Deep convection can lift ozone-depleted boundary layer air aloft, leading to reduced ozone concentrations in the upper troposphere. [*Folkins et al.,* 2002, 2006].

1.1.3 Nitrogen Oxide Emissions

NO_x is emitted in the troposphere primarily as NO, but a rapid cycling between NO and NO_2 leads to a quickly reached steady state. Anthropogenic activities provide the largest total source

of NO_x to the atmosphere, as NO_x is produced during the burning of fossil fuels during power generation and transportation. Estimates of the total anthropogenic NO_x source vary amongst different emissions inventories, but are generally around 30 Tg N a^{-1} [*Granier et al.*, 2011].

Natural NO_x emissions account for approximately 35% of the total NO_x source. The most significant source of NO_x to the upper troposphere is lightning. High temperatures created during lightning flashes lead to dissociation of diatomic nitrogen and oxygen molecules which combine to produce NO [*Borucki and Chameides,* 1984]. Modeling studies show that lightning NO_x emissions are the most important contributor to tropical upper tropospheric ozone and drive interannual variability of tropical ozone and OH [*Sauvage et al.*, 2007a,b; *Murray et al.*, 2013]. Lightning NO_x is also the main source of HNO_3 in the upper troposphere, as HNO_3 produced from surface sources is likely to be removed by precipitation in the lower troposphere [*Popp et al., 2009*]. Recent estimates of the total lightning NO_x source are 5 ± 3 Tg N a^{-1} [*Schumann and Huntrieser,* 2007] and 6.3 ± 1.4 Tg N a^{-1} [*Miyazaki et al.,* 2014].

Additional natural NO_x emissions include biomass burning and microbial activity in soils, which range from 6-12 Tg and 4-15 Tg N a^{-1} respectively [*Vinken et al.,* 2014].

1.2 Remote Sensing of Atmospheric Trace Gases

Remote sensing refers to measurement techniques that provide information on the state of the atmosphere without being in direct contact. These instruments measure the intensity of radiation emitted by the atmosphere at various wavelengths. Retrieval algorithms are employed to deduce the abundances of trace gases given their known spectral features.

Satellite instruments can provide information on the state of the atmosphere with greater spatial and temporal resolution than can be achieved from in situ measurements. This allows for

the study of atmospheric processes that drive composition at large regional or global scales that were previously difficult to observe.

Observations from several satellite instruments are used in this thesis. These instruments have varying observational geometry and measurement techniques. Nadir viewing instruments have a downward facing viewing angle and can provide information about the column of atmosphere observed with limited vertical information. IASI, a nadir viewing instrument used in this thesis, employs a Fourier Transform Spectrometer to measure thermal infrared radiation emitted in the observed column of atmosphere. Limb viewing and solar occultation instruments can provide vertical information about the atmosphere as they view a tangential path through the atmosphere. The Aura Microwave Limb Sounder (MLS), which observes thermal microwave radiation, and OSIRIS, which observes radiation ranging from ultraviolet to visible wavelengths, are limb viewing instruments used in this thesis. A solar occultation instrument, ACE-FTS, which observes thermal infrared radiation, is also used here. Information regarding these satellite instruments is summarized in Table 1-1.

Name	Launch Year	Viewing Geometry	Radiation Wavelengths Observed	Retrieved Trace Gases Used
MLS	2006	Limb	Thermal Microwave (0.12 – 2.5 mm)	O_3 (1.2 mm)
ACE-FTS	2004	Occultation	Thermal IR (7-13 μm)	O_3 (9.6 μm)
				HNO_3 (11 μm)
OSIRIS	2001	Limb	UV – VIS (280 – 800 nm)	O_3 (320-360 nm)
IASI	2004	Nadir	Thermal IR (3 - 15 μm)	HNO_3 (11 μm)
				CO (4.5 μm)
HIRDLS	2004	Limb	Thermal IR (6 – 18 μm)	HNO_3 (11 μm)

Table 1-1: Satellite instruments used in this work. Wavelengths of interest for retrieved trace gases are given in parentheses

1.3 Chemical Transport Models and Inverse Modeling

Remote sensing and in situ observations provide information on atmospheric composition. Chemical transport models are then useful to understand the processes that lead to this observed state of the atmosphere. Chemical transport models, such as the GEOS-Chem model used in this thesis, use meteorological data, emissions inventories, and equations describing advection, deposition, and chemical production and loss to provide a simulated state of atmospheric composition. Insight into atmospheric processes can be gained by performing sensitivity studies and comparing the simulated atmospheres to observations.

Emission inventories used in chemical transport models are typically derived from a combination of activity data (e.g. fuel consumption, lightning flash rates) and experimentally derived emission factors that estimate the quantity of NO_x produced per activity. These "bottom-up" inventories are prone to errors due to inaccurate reporting of emissions or uncertainties in emission factors [*Zhao et al.,* 2011]. "Bottom-up" inventories often take years to compile, and thus can quickly become out of date. An alternate method for estimating emission inventories is to use a "Top-down" approach that uses an inverse model to determine the emissions that would be necessary to account for the abundance of NO_2 as observed by satellite observations. One such "top-down" method is a mass balance method that assumes a linear relationship between NO_2 columns and local NO_x emissions, as introduced by *Martin et al.* [2003].

Another inverse modeling method is the use of an adjoint model. A typical chemical transport model begins with emission of chemical species which are then affected by physical and chemical mechanisms over time. An adjoint model begins with an observed chemical state of the atmosphere and propagates information backwards in time to infer the emissions and

processes that were necessary to create that state. Assimilating observational data into an adjoint model can help constrain emissions inventories.

1.4 Goals of this Work

O_3, HNO_3, and NO_x concentrations in the upper troposphere are influenced by many factors, including emissions, transport, and chemistry. This thesis brings together research that interprets satellite observations using a chemical transport model to examine each of these processes to better understand tropospheric composition and chemistry.

Deep convection can transport ozone-poor air from the marine boundary layer to the upper troposphere, diluting ozone concentrations aloft. This has been observed in ozonesonde observations [*Kley et al.*, 1996; *Solomon et al.*, 2005]. In Chapter 2, these upper tropospheric low ozone events are observed for the first time from space using the Microwave Limb Sounder (MLS) satellite instrument. The superior spatial extent of satellite observations relative to ozonesondes allowed for examination of the spatial distribution and frequency of these events. We also examine the effects that important oscillations in tropical convection have on these events. This work was published in *Geophysical Research Letters* in 2013.

NO_x produced by lightning is an important source of ozone production in the free troposphere. Lightning NO_x emission is a sub-grid scale problem that must be parameterized in a chemical transport model. As upper tropospheric HNO_3 is sensitive to lightning NO_x emissions, the lightning NO_x parameterization can be evaluated using observations of HNO_3. This is the goal the research presented in Chapter 3. Comparisons between HNO_3 observations from the IASI satellite instrument and those simulated by GEOS-Chem indicated a bias in HNO_3 over Southeast Asia that was attributed to deficiencies in the lightning NO_x parameterization in the model. Sensitivity studies on several aspects of the lightning parameterization highlight the

7

importance of lightning to upper tropospheric composition. This work was published in the *Journal of Geophysical Research: Atmospheres* in 2014.

NO_x emission inventories used in chemical transport models have significant uncertainties that hinder research on NO_x chemistry. Satellite observations can be used to provide a "top-down" constraint to improve these inventories. An inversion model is needed to obtain information on the emissions that are necessary to produce the observed concentrations. In Chapter 4, the GEOS-Chem adjoint model is used as a benchmark for evaluating the accuracy of mass balance inversion methods using synthetic observations of NO_2 columns. Improvements upon the often used mass balance methodology are tested, including iterative methods and the addition of a scaling factor determined using finite difference. The goals of this work were to improve mass balance inversion performance, and to compare the abilities of mass balance and adjoint inversions.

Chapter 2: Analysis of Satellite Remote Sensing Observations of Low Ozone Events in the Tropical Upper Troposphere and Links with Convection

Authors: Matthew J. Cooper[1], Randall V. Martin[1,2], Nathaniel J. Livesey[3], Doug A. Degenstein[4], Kaley A. Walker[5,6]

1. Department of Physics and Atmospheric Science, Dalhousie University, Halifax NS Canada

2. Harvard-Smithsonian Center for Astrophysics, Cambridge MA USA

3. Jet Propulsion Laboratory, California Institute of Technology, Pasadena CA USA

4. Department of Physics and Engineering Physics, Institute of Space and Atmospheric Science, University of Saskatchewan, Saskatoon SK Canada

5. Department of Physics, University of Toronto, Toronto ON Canada

6. Department of Chemistry, University of Waterloo, Waterloo ON Canada\

2.1 Abstract: Satellite observations from three instruments (MLS, OSIRIS, ACE-FTS) reveal coherent patterns of low ozone events (<20 ppbv) in the tropical upper troposphere. Using a chemical transport model (GEOS-Chem) we find that these events result from deep convective processes that rapidly transport air with low ozone concentrations from the marine boundary layer. These events occur with greater frequency over the tropical South Pacific warm pool, which is consistent with ozonesonde observations. The satellite observations indicate spatial

shifts in the frequency of low ozone events that we attribute to changes in convection. As the location of the warm pool shifts eastward during El Niño events, the location of the most frequent low ozone events in the satellite record follows. Mapping of low ozone events over time reveals eastward propagating systems resembling the Madden-Julian Oscillation. These observations and analyses strengthen the link between deep convection and ozone concentrations in the tropical upper troposphere.

2.2 Introduction

Ozone (O_3) is an important contributor to upper tropospheric oxidation processes and radiative forcing [*Lacis et al.,* 1990; *Thompson*, 1992]. Upper tropospheric ozone is greatly affected by convection in addition to the chemical production and loss mechanisms [*Folkins et al.*, 2002; *Sekiya and Sudo*, 2012]. Dynamic processes in the tropics vary on weekly, seasonal and interannual timescales leading to variability in ozone concentrations. Strengthening scientific understanding about the link between convection and upper tropospheric ozone concentrations is essential to understand ozone and its variability.

The tropical marine boundary layer is a region with intense solar radiation and high humidity. Under these condition an O_3 molecule is easily photolyzed and the resulting excited oxygen atom readily reacts with water vapor, leading to a net loss of O_3 [*Johnson et al.*, 1990]. This leads to O_3 concentrations reaching values as low as a few ppbv in the clean tropical marine boundary layer [*Kley et al.*, 1996]. Deep convection in the tropics is believed to bring this air with low ozone concentrations to the upper troposphere causing reduced ozone columns [*Folkins et al.,* 2002]. The resulting depletion in ozone concentrations has been observed by ozonesondes in a few convectively active regions [*Kley et al.,* 1996; *Solomon et al.,* 2005]. However, the spatial extent of these events remains weakly quantified.

Interannual variability of tropical convection is largely driven by the El Niño-Southern Oscillation (ENSO). During El Niño events, warming of the central and eastern Pacific Ocean leads to significant changes in the strength and distribution of convective events as a result of the strong link between convection and surface temperatures. A recent study by *Oman et al.* [2013] used satellite observations and a chemistry-climate model to describe the sensitivity of mean upper tropospheric ozone concentrations to ENSO.

The Madden-Julian Oscillation (MJO) is the dominant source of seasonal variability in the tropics [*Madden and Julian,* 1994]. The MJO is identified by extensive regions of enhanced convection that form over the Indian Ocean and propagate eastward along the equator with a period of 40-50 days. Ozone anomalies connected to the MJO have been previously observed in O_3 column data from satellites [*Ziemke and Chandra,* 2003; *Tian et al.,* 2007], but to our knowledge have not been observed in the upper troposphere.

Scientific understanding of the effects of convection on ozone in the upper troposphere has been inhibited by the paucity of observations. Ozonesondes have provided a glimpse into these connections at a few locations [*Kley et al.,* 1996; *Solomon et al.,* 2005; *Lee et al.,* 2010]. Satellite observations of column ozone yield hints about the global nature of these processes [*Shiotani,* 1992; *Ziemke et al.,* 2010; *Chae et al.,* 2011], but without specificity to the upper troposphere. Here we apply satellite observations of upper tropospheric ozone to detect convectively driven low ozone events from space at unprecedented spatial and temporal scales, and to analyze these events with a chemical transport model.

2.3 Data

We use satellite observations in three spectral regions (microwave, ultraviolet-visible, and mid-infrared) to observe low ozone events, and reduce the chance of artifacts affecting our conclusions. The Aura Microwave Limb Sounder (MLS) is a thermal-emission microwave limb

sounding instrument launched in July 2004. MLS makes 3500 profile measurements from the upper troposphere to the mesosphere with a horizontal spacing of 165 km daily. In this study we use version 3.3 of the MLS data processing algorithms for retrievals between August 2004 and January 2012 [*Livesey et al.,* 2011]. The wavelengths of the measured radiation are such that thin and moderate clouds do not affect the retrievals, however thick clouds may affect the retrievals. We ignore any measurements which may have been influenced by clouds through the recommended screening processes using the MLS data quality flags. Comparisons between MLS O_3 and ozonesondes show the best agreement (better than 10%) in the tropical upper troposphere at 215 hPa with small positive biases (<10 ppbv over the Pacific), but indicate larger biases at other pressure levels [*Livesey et al.,* 2012].

The Optical Spectrograph and InfraRed Imaging System (OSIRIS) was launched in 2001 and measures scattered sunlight in the limb with wavelengths ranging from ultraviolet to infrared (280 to 800 nm) [*Llewellyn et al.,* 2004; *McLinden et al.,* 2012]. Daily observations are made between 6 and 60 km with a horizontal resolution of 500 to 1000 km and a vertical resolution of 2 km. This study uses the SaskMART ozone product version 5-07 for orbits occurring between October 2001 and June 2012 [*Degenstein et al.,* 2009]. Annual mean OSIRIS O_3 concentrations agree with in situ observations to within 5% in the tropical upper troposphere, although seasonal biases are larger and high altitude clouds may cause retrieval errors [*von Savigny et al.,* 2005; *Cooper et al.,* 2011].

The Atmospheric Chemistry Experiment Fourier Transform Spectrometer (ACE-FTS) is a solar occultation instrument launched in August 2003 measuring infrared radiation (750 - 4400 cm^{-1}) providing a few hundred ozone profiles per year in the tropics [*Bernath et al.*, 2006]. Ozone observations are made between the cloud tops and 95 km with a vertical resolution of ~3

km and profiles are retrieved using a non-linear least squares fitting method [*Boone et al.*, 2005]. ACE-FTS version 3.0 profiles for measurements between February 2004 and September 2010 are used for this work. Annual mean ozone profiles generally agree with in situ observations, with a high bias of 10-13% in the tropical upper troposphere that increases with increasing pressure [*Cooper et al.*, 2011].

Ozonesonde measurements at Java (7°S, 111°E), Fiji (18°S, 178°E), Samoa (13°S, 171°W), Hilo (19°N, 155°W), San Cristobal (1°S, 89°W) and Natal (5°S, 35°W) are used here. These measurements are part of the Southern Hemisphere Additional Ozonesondes (SHADOZ, http://croc.gsfc.nasa.gov/shadoz/) network, a group of 16 ozonesonde sites in the southern tropics [*Thompson et al.,* 2003a, 2003b].

In this study we use the monthly mean Nino 3.4 index, based on sea surface temperatures (SST), to determine when El Niño and La Niña conditions occur. This index is available from the NOAA SST indices website (http://www.cpc.ncep.noaa.gov/data/indices/).

Outgoing longwave radiation (OLR) serves as an indicator of deep convection. Data are provided by the NOAA/OAR/ESRL PSD, Boulder, Colorado, USA, from their website (http://www.esrl.noaa.gov/psd/).

2.4 Results

Figure 2-1 shows the fraction of MLS soundings at the 215 hPa level that recorded low ozone concentrations (<20 ppbv). These low concentrations are less than half of the mean tropical upper tropospheric ozone concentrations of 50 ppbv. To our knowledge, this is the first map of low ozone event frequency. These low ozone events occur frequently in the tropical West Pacific and rarely occur elsewhere in the tropics. Figure 2-1 also shows a map of annual mean OLR for which lower values indicate regions with high clouds. A comparison of these plots shows some similar spatial features in tropical marine regions between the frequency of low

ozone events and high clouds, suggesting that these events have a convective origin. Although central Africa and South America are also regions with strong convection, boundary layer ozone concentrations over land tend to be higher than those over ocean and thus deep convection does not create as many low ozone events. The fractions shown in Figure 2-1 agree within 12% with frequencies calculated from ozonesonde measurements over 1998-2008 from three SHADOZ sites in the region (Samoa, Java and Fiji), and with similar ozonesonde analyses in previous studies [*Solomon et al.,* 2005]. Low ozone events occur exclusively within the pressure range of 100-300 hPa. The mean low ozone event frequency can vary by up to 20%.

We repeated this analysis using data from the ACE-FTS and OSIRIS instruments and found features similar to those seen by MLS. Although ozonesonde comparisons indicate that MLS O_3 is more accurate at 215 hPa than at 147 hPa in the tropics [*Livesey et al.,* 2012], we perform these comparisons at the 147 hPa level as errors in both ACE-FTS and OSIRIS increase with increasing pressure. Retrievals from all three satellites frequently show low ozone concentrations at 147 hPa over the tropical West Pacific (15°S-15°N, 100-180°E), with low ozone occurring in 11% of ~280,000 MLS, 11% of ~26,000 OSIRIS, and 12% of ~200 ACE-FTS retrievals. ACE-FTS and OSIRIS also observe low ozone concentrations less frequently in other regions, occurring in less than 5% of profiles elsewhere in the tropics. This is consistent with ozonesondes in Hilo, San Cristobal, and Natal, which also have O_3 concentrations less than 20 ppbv in fewer than 5% of profiles. It is unlikely that artifacts in the retrievals would produce such consistent errors, since each instrument measures radiation in a different spectral region.
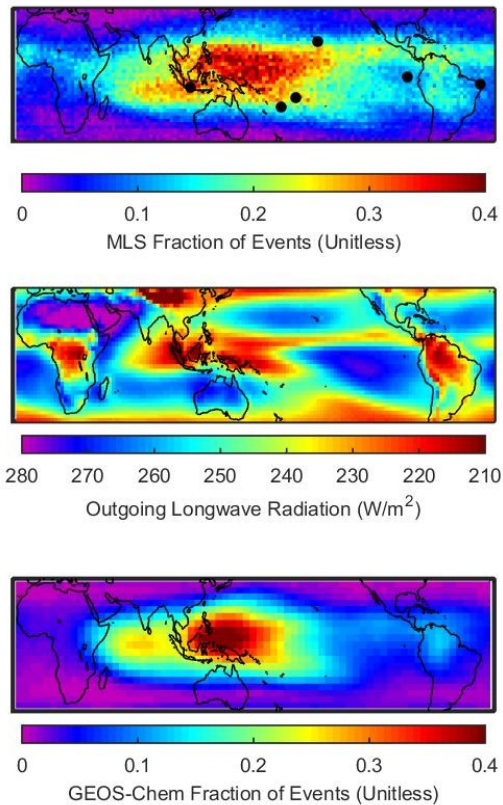
Figure 2-1: (Top) Frequency of low ozone events (<20 ppbv) at 215 hPa observed by the MLS satellite instrument over the years 2004-2012. Black dots indicate ozonesonde locations. (Middle) Observations of outgoing longwave radiation (OLR), for which low values indicate regions of deep convection. (Bottom) Frequency of low ozone events in a GEOS-Chem simulation for 2004-2010 with random Gaussian noise added to model output to simulate MLS measurement precision.

We use the chemical transport model GEOS-Chem v9-01-03 (see Chapter 2.7) to simulate low ozone events. The model is driven by assimilated meteorological fields from GEOS-5 for the years 2004-2010. We add Gaussian random noise ($\sigma = 20$ ppbv) to the simulated ozone profiles to mimic MLS measurement precision. Without this added noise, the model simulates the spatial distribution of low ozone events but underestimates the frequency by up to 25%. The simulated frequency of low ozone events with added noise is displayed in Figure 2-1.

The simulation reproduces the location of maximum frequency and has significant spatial agreement with MLS (r = 0.88). We focus our attention on the region of maximum frequency.

Lawrence et al. [2003] found a strong sensitivity of upper tropospheric ozone to deep convection. We tested the hypothesis that these events are convectively driven by performing a GEOS-Chem simulation without convection. The frequency of low ozone events decreases relative to the standard simulation a few days after convection ceases, leading to a 15% increase in upper tropospheric O_3 concentrations. The simulated O_3 chemical production and loss rates change by less than 5%, which is insufficient to explain the upper tropospheric O_3 concentration changes over a few days. Thus the decreasing frequency of low ozone events and resulting O_3 concentration increase can only be explained by the lack of transport of ozone poor air from the boundary layer.

Previous analysis has attributed interannual variability in upper tropospheric ozone concentrations from MLS to dynamical variability due to the ENSO circulation [*Livesey et al.,* 2012; *Oman et al.,* 2013]. We further explore these low ozone events by separating the MLS retrievals into two groups representing either El Niño or La Niña conditions based upon the monthly mean Nino 3.4 index. Figure 2-2 shows the resulting change in low ozone event frequency. Low ozone events over the East Pacific occur almost twice as frequently during an El Niño (increasing from 8% to 15% over 15°N-15°S, 180-100°W). This shift in the frequency of low ozone events mirrors the shift of the warm sea surface temperatures that occurs during El Niño events.
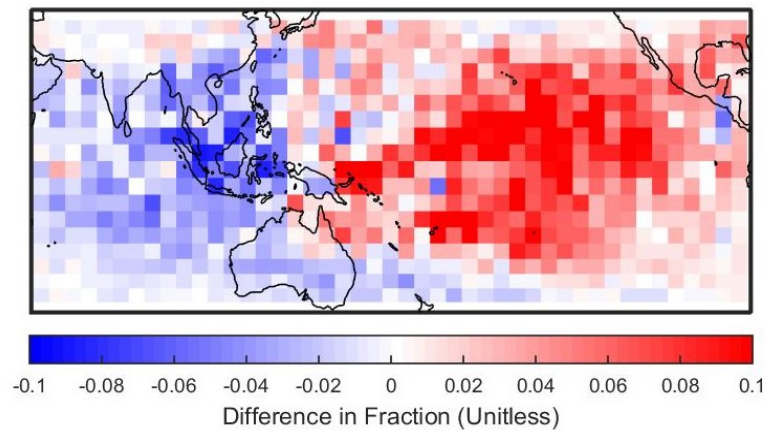
Figure 2-2: Difference in deseasonalized frequency of low ozone events between El Niño and La Niña conditions over years 2004-2012. El Niño (La Niña) conditions are defined using Nino 3.4 SST anomaly of greater than 0.4 (less than -0.4) K.

Low ozone events occur more frequently over the East Pacific during El Niño conditions, and more frequently over the West Pacific during La Niña. Table 2-1 shows that a shift similar to that seen by MLS is also evident in observations from the ACE-FTS and OSIRIS satellite instruments, and in comparisons between ozonesondes in the East Pacific (Samoa) versus those in the West (Java). Uncertainties in the values given in Table 2-1 were estimated using the measurement precision for each instrument. The fraction of low ozone events found in all three satellites generally agree within their uncertainties. The frequency change observed by the satellite instruments due to ENSO is similar to that seen in the ozonesonde record, although positive biases in the satellite ozone retrievals may lead to fewer low ozone events meeting the 20 ppbv threshold. GEOS-Chem simulations for El Niño and La Niña years show an increase in low ozone event frequency over the central Pacific during El Niño, but do not fully reproduce the observed decrease in frequency over the West Pacific since the GEOS-5 meteorological fields do not significantly decrease convective activity in that region.

		East Fraction	East Number	West Fraction	West Number	Difference
MLS	El Niño	16±4	66,000	11±3	59,000	5±5
	La Niña	8±3	122,000	14±3	92,000	-6±4
OSIRIS	El Niño	26±2	6,000	14±3	6,000	12±4
	La Niña	14±3	8,000	16±4	7,000	-2±5
ACE-FTS	El Niño	26±9	27	13±8	16	13±12
	La Niña	5±3	41	19±12	16	-14±12
Ozonesondes	El Niño	28±5	53	17±5	91	11±7
	La Niña	11±3	109	31±4	161	-20±5

Table 2-1: Percentage of measurements at 145 hPa with ozone concentrations less than 20 ppbv. Total number of observations in each region also shown. West Pacific is bounded by (15°S - 15°N, 70°E - 140° E) and East Pacific is bounded by (15°S - 15°N, 110°W – 180°W). Ozonesonde measurements from Samoa (Java) are used for East (West) Pacific. Difference values are for East Pacific Fraction minus West Pacific Fraction

In Figure 2-3 we test the hypothesis that larger temperature changes associated with stronger El Niño events have larger effects on convective frequency. Each dot represents a three month sliding average of the deseasonalized frequency of low ozone events in the MLS record over the East or West Pacific plotted against the Nino 3.4 SST anomaly. A statistically significant correlation (p-values less than 10^{-7}) is evident between the value of the Nino 3.4 SST anomaly and the frequency of low ozone events on both sides of the Pacific. A large positive SST anomaly value indicates El Niño conditions, which leads deep convection to occur more frequently over the East Pacific and less frequently over the West. The slopes of the best fit lines indicate that the frequency of low ozone events is strongly related to the strength of the ENSO events.
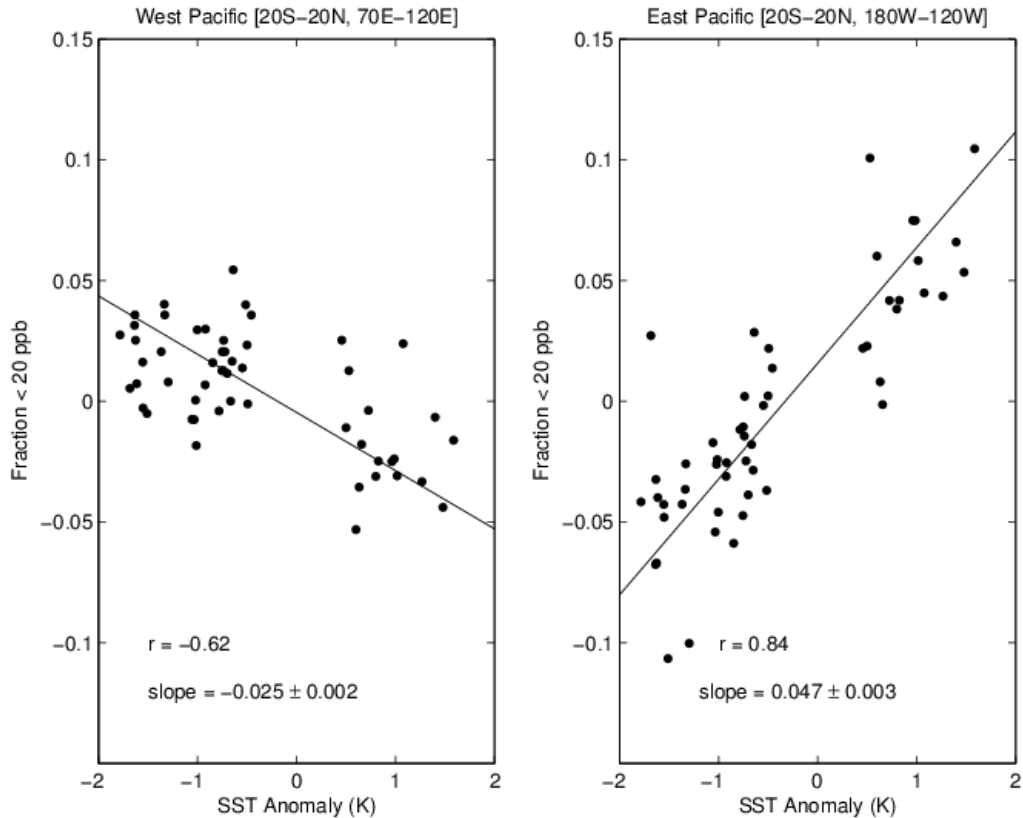
Figure 2-3: Scatter plot showing deseasonalized frequency of low ozone events versus Nino 3.4 sea surface temperature anomaly. Each dot represents a 3 month sliding average of MLS values. Only points during El Niño or La Niña conditions are shown. The slope and uncertainty of the best fit lines were found by a reduced major axis regression [*Miller and Kahn,* 1962].

MJO signals are also visible in the MLS ozone record. The Hovmöller diagram in Figure 2-4 shows the low ozone event frequency as a function of time and longitude over the tropical Indian and Pacific oceans. Event frequency is calculated for five day intervals over latitudes spanning 15°S-15°N. We observe that regions with frequent low ozone events form over the Indian Ocean and travel eastward across the Pacific in a manner resembling similar diagrams made using outgoing longwave radiation measurements during the MJO [*Wong and Dessler,* 2007]. The eastward-moving patterns occur with a period of 1-2 months, and we calculate an average propagation speed of 5 m/s. These values match those typical measured of MJO. The

19

GEOS-Chem simulation partially resolved eastward-moving patterns of low ozone frequency but further development of the meteorological fields appears needed.
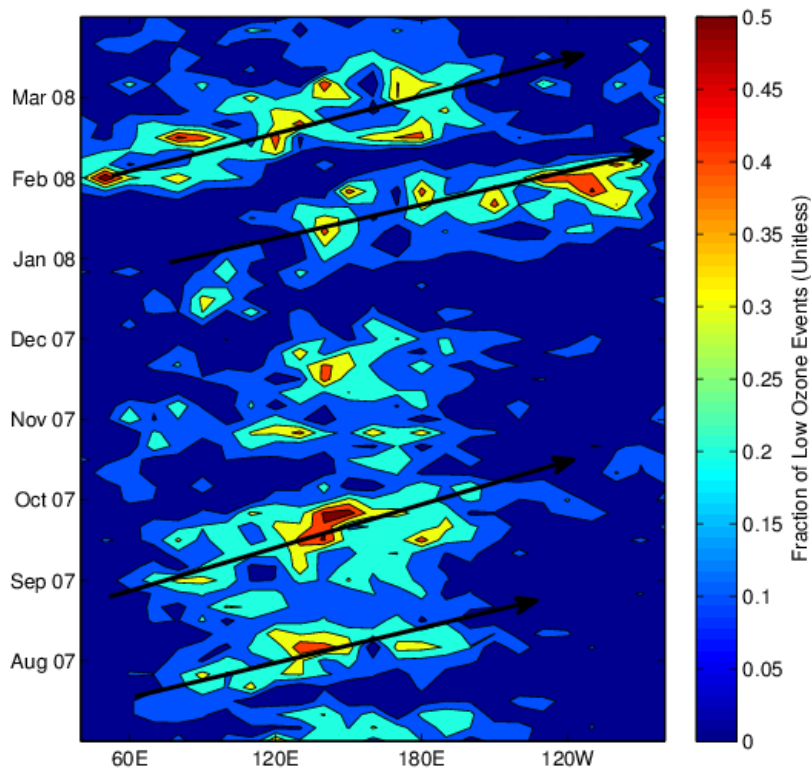
Figure 2-4: Hovmöller diagram displaying the low ozone event frequency from MLS over the Indian and Pacific Oceans (15°S – 15°N) for the period of August 2007 – March 2008. Areas of frequent low ozone events move eastward at ~5 m/s, in a repeating pattern with a period of 1-2 months, following the Madden-Julian Oscillation.

2.5 Conclusion

Coherent spatial and temporal patterns of ozone concentrations less than 20 ppbv in the tropical upper troposphere are observed for the first time with the MLS, ACE-FTS, and OSIRIS satellite instruments. These low ozone events occur most frequently in the convectively active region of the West Pacific warm pool with spatial patterns that resemble outgoing longwave radiation. The MLS, ACE-FTS and OSIRIS satellite instruments observe low ozone events in 15-25% of ozone profiles in this region, which agrees with values in the ozonesonde record. Both satellite and ozonesonde observations indicate shifts in low ozone events over the Pacific

20

Ocean related to the ENSO circulation, with more frequent events over the central Pacific when the ocean beneath warms during El Niño conditions. On shorter timescales, regions with frequent low ozone events propagate eastward through the tropics with period and velocity typical to the MJO. Results from a state-of-the-science chemical transport model (GEOS-Chem) support the hypothesis that the events result from deep convection. The model was able to simulate the structure of the most frequent low ozone events, but only partially reproduced the westward shift in low ozone event frequency during La Niña. Future effort to reproduce these features will require developments to convective parameterizations or assimilated meteorological fields. These observations provide a sensitive test of the ability of global models to represent the coupling of chemical and dynamical processes of relevance to climate.

2.7 Supporting Information: Description of the GEOS-Chem model

The GEOS-Chem global 3-D chemical transport model [*Bey et al.,* 2001] is used in this study. Version 9-01-03 (http://geos-chem.org) is used here at a horizontal resolution of 4°x5°. The model is described on 47 vertical levels, extending from the surface to 0.1 hPa including approximately 35 levels in the troposphere.

GEOS-Chem contains a detailed simulation of HO_x-NO_x-VOC-O_3-aerosol chemistry. The current chemical mechanism in GEOS-Chem includes the most recent JPL/IUPAC recommendations as implemented into GEOS-Chem by *Mao et al.* [2010]. The stratospheric ozone simulation uses the Linoz algorithm of *McLinden et al.* [2000]. The global lightning NO_x

source is 6 Tg N a^{-1} [*Martin et al.*, 2007] and scaled to match OTD/LIS observations of lightning flashes as implemented in v9-01-03 by *Murray et al.* [2012].

The model is driven by assimilated meteorological data provided by the Global Modeling and Assimilation Office (GMAO) at NASA Goddard Space Flight Center. GEOS-5 meteorological fields for the years 2004-2010 are used here. GEOS-5 employs the relaxed Arakawa-Schubert convective parameterization for shallow and deep moist convection [*Moorthi and Suarez, 1992*]. Comparisons of mass divergence profiles indicate that the level of maximum convective outflow in GEOS-5 agrees well with observations [*Mitovski et al.,* 2011].

GEOS-Chem has been used in several recent studies of tropospheric ozone [*Parrington et al.,* 2012; *Cooper et al.,* 2011; *Nassar et al.,* 2009]. The O$_3$ simulation has been extensively evaluated against in situ measurements [*Zhang et al.*, 2010; *Nassar et al.*, 2009; *Sauvage et al.*, 2007a]. The GEOS-Chem fields generally reproduce changes in the tropospheric ozone column associated with El Niño [*Chandra et al.,* 2002, 2003].

Chapter 3: Tropospheric Nitric Acid Columns from the IASI Satellite Instrument Interpreted with a Chemical Transport Model: Implications for Parameterizations of Nitric Oxide Production by Lightning

Matthew Cooper[1], Randall V. Martin[1,2], Catherine Wespes[3], Pierre-Francois Coheur[3], Cathy Clerbaux[3,4], Lee T. Murray[5]

1. Department of Physics and Atmospheric Science, Dalhousie University, Halifax, Nova Scotia, Canada.

2. Harvard-Smithsonian Center for Astrophysics, Cambridge, Massachusetts, USA

3. Spectroscopie de l'Atmosphère, Chimie Quantique et Photophysique, Université Libre de Bruxelles, Brussels, Belgium

4. Sorbonne Universités, UPMC Univ. Paris 06; Université Versailles St-Quentin; CNRS/INSU, LATMOS-IPSL, Paris, France

5. NASA Goddard Institute for Space Studies and Lamont-Doherty Earth Observatory of Columbia University, New York, USA

3.1 Abstract

This paper interprets tropical tropospheric nitric acid columns from the IASI satellite instrument with a global chemical transport model (GEOS-Chem). GEOS-Chem columns generally agree with IASI over the tropical ocean to within 10%. However the GEOS-Chem simulation underestimates IASI nitric acid over Southeast Asia by a factor of two. The regional nitric acid bias is confirmed by comparing the GEOS-Chem simulation with additional satellite (HIRDLS, ACE-FTS) and aircraft (PEM-Tropics A and PEM-West B) observations of the middle and upper troposphere. This bias is likely driven by the lightning NO_x parameterization, both in terms of the magnitude of the NO_x source and the ozone production efficiency of concentrated lightning NO_x plumes. We tested a subgrid lightning plume parameterization and found that an ozone

production efficiency of 15 mol/mol in lightning plumes over Southeast Asia in conjunction with

an additional 0.5 Tg N would reduce the regional nitric acid bias from 92% to 6% without

perturbing the rest of the tropics. Other sensitivity studies such as modified NO_x yield per flash,

increased altitude of lightning NO_x emissions, decreased convective mass flux, or increased

scavenging of nitric acid required unrealistic changes to reduce the bias.

3.2 Introduction

Nitrogen oxides ($NO_x \equiv NO + NO_2$) in the free troposphere largely control the production

of ozone (O_3), an important greenhouse gas and atmospheric oxidant. The dominant sink for NO_x

is oxidation to nitric acid (HNO_3). HNO_3 is one of the main forms of reactive nitrogen (NO_y) in

the free troposphere, representing up to 50% of NO_y in the tropical upper troposphere

[*Kasibhatla et al.*, 1993; *Folkins et al.*, 2006]. However, models generally have difficulty

reproducing observed NO_x/HNO_3 ratios [*Brunner et al.,* 2005; *Singh et al.,* 2007]. Improved

understanding of HNO_3 production and loss mechanisms can help to better constrain NO_x

emissions, and in turn improve understanding of ozone production and its effect on climate.

Direct measurements of free tropospheric HNO_3 are rare, particularly in the tropics.

HNO_3 measurements taken during aircraft campaigns offer high precision but have limited

spatial and temporal coverage. Satellite instruments are capable of providing superior temporal

and spatial sampling in the tropics. HNO_3 concentrations have been retrieved from observations

from several satellite instruments, including LIMS [*Gille et al.,* 1984], MIPAS [*Tsidu et al.,*

2005], MLS [*Santee et al.,* 2004], ACE-FTS [*Wolff et al.,* 2008], and HIRDLS [*Kinnison et al.,*

2008]. However these instruments are primarily focused on high latitudes or stratospheric

altitudes. In this study we use the Infrared Atmospheric Sounding Interferometer (IASI)

instrument on the MetOp satellite platform. IASI is a high resolution spectrometer that provides

global observations of HNO$_3$ column abundances with an unprecedented spatial and temporal resolution [*Wespes et al.,* 2009].

Lightning NO$_x$ has a large influence on tropospheric ozone and nitric acid as lightning NO$_x$ is emitted directly into the free troposphere where NO$_x$ lifetimes are longer [*Liu et al.,* 1987; *Pickering et al.,* 1990; *Sauvage et al.,* 2007b]. Best estimates of the global lightning NO$_x$ source range from 2-8 Tg N a^{-1} but significant uncertainty remains in both the magnitude and vertical and horizontal distribution of the source [*Martin et al.,* 2007; *Schumann and Huntrieser,* 2007]. A difficulty in modeling the effects of lightning NO$_x$ is that lightning is a sub-grid scale process which must be parameterized in chemical transport models. Lightning parameterizations are most often based on meteorological properties and are sensitive to the convection scheme used in the model [*Tost et al.,* 2007; *Koshak et al.,* 2013]. Lightning NO$_x$ production is often determined using a prescribed number of NO$_x$ molecules produced per flash, but this value varies significantly between models [*Schumann and Huntrieser,* 2007]. O$_3$ and HNO$_3$ concentrations are sensitive to the vertical placement of lightning NO$_x$ emissions [*Labrador et al.,* 2005]. Uncertainty also arises when considering the dispersion rate of lightning NO$_x$ plumes as rates of chemical reactions vary nonlinearly with respect to NO concentrations [*Lin et al.,* 1988]. Since HNO$_3$ is highly soluble and is quickly scavenged in convective updrafts, HNO$_3$ concentrations are sensitive to convective mixing and wet deposition in models [*Giorgi and Chameides,* 1986; *Mari et al.,* 2000; *Staudt et al.,* 2003].

The following paper examines tropical tropospheric HNO$_3$ columns retrieved from IASI satellite measurements. Chapter 3.3 describes data sources and other tools used in this work. Chapter 3.4 describes GEOS-Chem, a state-of-the-science global chemical transport model that is used here to interpret the IASI observations. Chapter 3.5 describes how GEOS-Chem is used

to investigate the ability of IASI to provide information about HNO_3 in the tropical troposphere. In the process of this evaluation a bias in the GEOS-Chem HNO_3 simulation over the tropical West Pacific and Indian Oceans is discovered. Chapter 3.6 discusses several possible methods for resolving the bias, including changes to wet deposition and lightning processes.

3.3 Observational Data

IASI was launched on the MetOp satellite in October 2006, into a polar sun-synchronous orbit with an equator crossing time of 9:30 AM and PM [*Clerbaux et al.*, 2009]. IASI is a nadir viewing Fourier transform spectrometer measuring thermal infrared radiation between 645 and 2760 cm^{-1}. HNO_3 and CO profiles are retrieved with the FORLI (Fast Operational/Optimal Retrievals on Layers for IASI) processing chains set up by the ULB/LATMOS groups [*Hurtmans et al.,* 2012]. The IASI HNO_3 retrievals have ~1 degree of freedom of signal (DOFS) providing a total column for HNO_3 offering no vertical information, except in the tropics where the DOFS reaches 1.5 [*Wespes et al.,* 2009; *Hurtmans et al.,* 2012]. IASI provides global coverage twice daily. Both day and night observations are used here. IASI scans across track either side of the nadir, with a total swath of around 2000 km. Each field of view is composed of four circular pixels of 12 km diameter at nadir. IASI's vertical sensitivity to HNO_3 is largest in the upper troposphere and lower stratosphere (approximately between 15 and 30 km) with weak sensitivity near the surface. The lower tropospheric sensitivity is stronger in the tropics than in mid- and polar latitudes because of higher surface temperatures [*Clerbaux et al.,* 2009]. Evaluation of previous IASI HNO_3 columns indicates average errors ranging from 12% at middle to high latitudes up to 32% near the equator [*Wespes et al.,* 2009; *Hurtmans et al.,* 2012]. The error is larger in the tropics due to stronger interferences with water vapour lines. Cloud information from the Eumetcast operational processing is used to reject observations with cloud coverage above 25%. IASI CO has been demonstrated to be a performant product in terms of

sensitivity (DOFS larger than 2 in the tropics) and retrieval errors (lower than 10% in the tropics). Evaluation of IASI CO columns show discrepancies of about 7% compared to other satellite instruments [*George et al.,* 2009]. HNO_3 and CO columns for the year 2008 are used in this study.

HNO$_3$ observations from two other satellites, the High Resolution Dynamics Limb Sounder (HIRDLS) on the Aqua satellite and the Atmospheric Chemistry Experiment Fourier Transform Spectrometer (ACE-FTS), are used for vertical profile information. HIRDLS is a limb scanning IR filter radiometer launched in 2004 on a near polar sun-synchronous orbit [*Kinnison et al.*, 2008]. The vertical resolution in the tropical upper troposphere is approximately 1 km. Individual profile precision in the retrieval is 10-15% but comparisons indicate a low bias of up to 30% relative to ACE-FTS and MLS satellite HNO_3 observations [*Kinnison et al.*, 2008]. Observations from 2005 to 2008 are used here. ACE-FTS is a solar occultation instrument measuring infrared radiation [*Bernath et al.,* 2005]. Its orbit is optimized for high latitudes and thus provides infrequent observations in the tropics, however complete coverage can be achieved if averaged over several years. Previous evaluation of ACE-FTS with aircraft measurements and the GEOS-Chem model indicates a positive bias in HNO_3 of 15% in the tropical upper troposphere [*Cooper et al.,* 2011]. Observations from 2004 to 2011 are used here.

We also use aircraft data from two of NASA's Pacific Exploratory Mission campaigns to evaluate the HNO_3 simulation. The West Phase B (PEM-West B) consisted of 16 flights by the NASA DC-8 over the northwest Pacific Ocean in February-March 1994 [*Hoell et al*., 1997]. The Tropics Phase A (PEM-Tropics A) also used the DC-8 aircraft for 17 flights throughout the tropical Pacific between New Zealand and Hawaii from August-September 1996 [*Hoell et al.*, 1999]. Individual HNO_3 measurement accuracy is reported as 30-35% [*Hoell et al.*, 1999].

Ozonesonde measurements at Kuala Lumpur (2.7° N, 101.7° E) are also used to evaluate the ozone simulation. These measurements are part of the Southern Hemisphere Additional Ozonesondes (SHADOZ, http://croc.gsfc.nasa.gov/shadoz/) network, a group of 16 ozonesonde sites in the southern tropics [*Thompson et al.,* 2003a, 2003b]. A total of 235 ozone profiles taken from the years 1998-2007 are used here.

3.4. GEOS-Chem

The GEOS-Chem global 3-D chemical transport model [*Bey et al.,* 2001] version 9-01-03 (http://geos-chem.org) is used to interpret the IASI HNO_3 observations. GEOS-Chem is driven by assimilated meteorological data provided by the Global Modeling and Assimilation Office (GMAO) at NASA Goddard Space Flight Center. GEOS-5 meteorological fields for the year 2008 degraded to a horizontal resolution of 4°x5° are used here. The GEOS-Chem simulation has 47 vertical levels, extending from the surface to 0.1 hPa including approximately 35 levels in the troposphere. GEOS-5 employs the relaxed Arakawa-Schubert convective parameterization for shallow and deep moist convection [*Moorthi and Suarez,* 1992].

GEOS-Chem contains a detailed simulation of HO_x-NO_x-VOC-O_3-aerosol chemistry in the troposphere, including the most recent JPL/IUPAC recommendations as implemented into GEOS-Chem by *Mao et al.* [2010]. The global lightning NO_x source of 6 Tg N a^{-1} was constrained using satellite and ozonesonde observations [*Martin et al.*, 2002; 2007] and is consistent with the 5.5 ± 2.0 Tg N a^{-1} used in current models [*Stevenson et al.,* 2013] and more recent top-down estimates from satellite observations of 6.3 ± 1.4 Tg N a^{-1} [*Miyazaki et al.,* 2014]. NO_x is distributed within simulated deep convection in a manner consistent with satellite climatologies of lightning flashes as described by *Murray et al.* [2012]. Lightning NO_x emissions are distributed relative to the cloud top height according to profiles based on aircraft observations and 3-D cloud-scale model simulations [*Ott et al.,* 2010]. Anthropogenic NO_x sources are from

the Emission Database for Global Atmospheric Research (EDGAR) inventory [*Olivier et al., 2005*] and overwritten by regional inventories in the northern midlatitudes. Biomass burning emissions are from the Global Fire Emissions Database (GFED v3) [*van der Werf et al.*, 2010]. The stratospheric ozone simulation uses the Linoz algorithm of *McLinden et al.* [2000]. Monthly mean production rates and loss frequencies for other gases in the stratosphere are computed using archived data from the GMI model [*Murray et al., 2013*]. The wet deposition scheme used in GEOS-Chem is described in *Liu et al.* [2001] with updates to subgrid scavenging by *Wang et al.* [2013]. HNO$_3$ is highly soluble and is often completely scavenged within the convective updraft [*Mari et al., 2000*].

3.5. Interpreting IASI Tropospheric HNO$_3$ Columns and Results

A major challenge in inferring tropospheric HNO$_3$ columns from IASI observations is determining which portion of the column can be attributed to the troposphere. The coarse vertical sensitivity of IASI makes this difficult, as tropospheric HNO$_3$ features are smoothed in the retrieval such that they overlap into the stratosphere and vice versa.

In the comparisons that follow, GEOS-Chem (GC) profiles are smoothed using the IASI averaging kernels to simulate IASI's coarse vertical resolution. A separate averaging kernel is used for each GC grid box. This is done using the method developed by *Rodgers and Conner* [2003]:

$$x'_{GC} \approx x_a + A(x_{GC} - x_a) \qquad (3 - 1)$$

where x_{GC} is the vertical HNO$_3$ profile from GEOS-Chem, x_a is the a priori profile used in the IASI retrievals, A is the IASI averaging kernel matrix, and x'_{GC} is the smoothed GEOS-Chem profile. The smoothed profile is then summed vertically to give a column value which can be compared to columns retrieved from IASI. A similar method of smoothing GEOS-Chem with

remote sensing instrument averaging kernels to examine tropospheric ozone was used by *Zhang et al.* [2010].

For consistency with IASI, we first scaled the GEOS-Chem stratospheric HNO_3 production and loss rates such that the smoothed total HNO_3 column over the remote Pacific Ocean (20°S - 20°N, 140° - 180° W) matches the IASI column. Over the remote tropical Pacific Ocean tropospheric HNO_3 concentrations are a small fraction (10%) of the total column abundance, and thus the column can be treated as primarily stratospheric. Zonal symmetry in stratospheric HNO_3 concentrations then allows this scaling to be applied throughout the tropics. This results in a 25% average reduction in smoothed total simulated HNO_3 columns across the tropics.

We use GEOS-Chem to aid the separation of the stratospheric and tropospheric columns. Stratospheric columns in GEOS-Chem are calculated by setting the simulated tropospheric concentrations to zero before smoothing the simulated profiles with the IASI averaging kernels:

$$x'_{GC\_strat} \approx x_a + A\left(x_{GC(troposphere=0)} - x_a\right) \qquad (3 - 2)$$

The tropospheric columns are then calculated by subtracting the smoothed GEOS-Chem stratospheric columns from both the smoothed model total columns and the IASI total columns (Ω_{IASI}):

$$Smoothed\ GC\ Tropospheric\ Column = \sum_{z=0}^{\infty} x'_{GC} - \sum_{z=0}^{\infty} x'_{GC\_strat} \qquad (3 - 3)$$

$$IASI\ Tropospheric\ Column = \Omega_{IASI} - \sum_{z=0}^{\infty} x'_{GC\_strat} \qquad (3 - 4)$$

where z is altitude. Potential errors in the GEOS-Chem tropospheric column over the remote

tropical Pacific may contribute to offset in the IASI tropospheric columns, but that offset would

cancel in the difference (IASI minus GEOS-Chem) on which we focus below.

Figure 3-1 shows the effect of smoothing GEOS-Chem with the IASI averaging kernel.

As IASI is most sensitive to the stratosphere and has coarse vertical resolution, the smoothing

enhances the stratospheric component relative to the tropospheric component, leading to an

apparent average reduction in the tropospheric column of 37%. This value is independent of the

scaling of the stratosphere and describes a source of uncertainty in the IASI tropospheric

columns due to the instrument's vertical sensitivity. The bottom row of Figure 3-1 shows that the

broad spatial patterns are retained in the smoothed tropospheric columns.
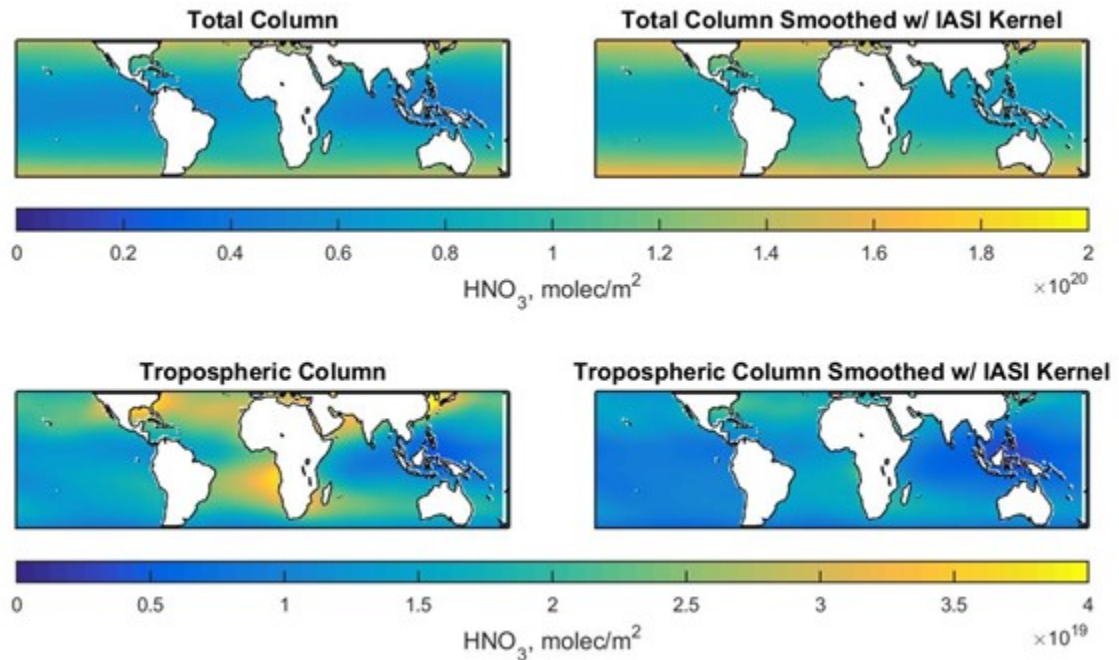
Figure 3-1: GEOS-Chem simulated HNO_3 columns. Subplots contain the total column, total column after smoothing with IASI averaging kernels, tropospheric column, and tropospheric column after smoothing with IASI averaging kernels.

Figure 3-2 shows annual mean tropospheric HNO_3 columns from IASI and GEOS-Chem. Emissivity features over deserts cause overestimations in the IASI columns [*Wespes el al.,* 2009], and while this problem is largely confined to desert regions we have ignored all observations over land as a precaution. GEOS-Chem is generally consistent with IASI over the tropics with a mean difference of 15% and a similar spatial distribution. Low concentrations over the Pacific Ocean and elevated concentrations over the tropical Atlantic are visible in both IASI and GEOS-Chem. However, IASI columns are up to twice as high as those in the simulation over the Indian Ocean and West Pacific Ocean regions (defined by 60°-160° E, 15°S-15°N, here referred to as Southeast Asia), and the Atlantic/Pacific contrast is stronger in the simulation.. This bias exists throughout the year. As measurement errors in the IASI retrievals are not higher in this region than elsewhere in the tropics [*Hurtmans et al.,* 2012], the simulation is the likely source of the bias.
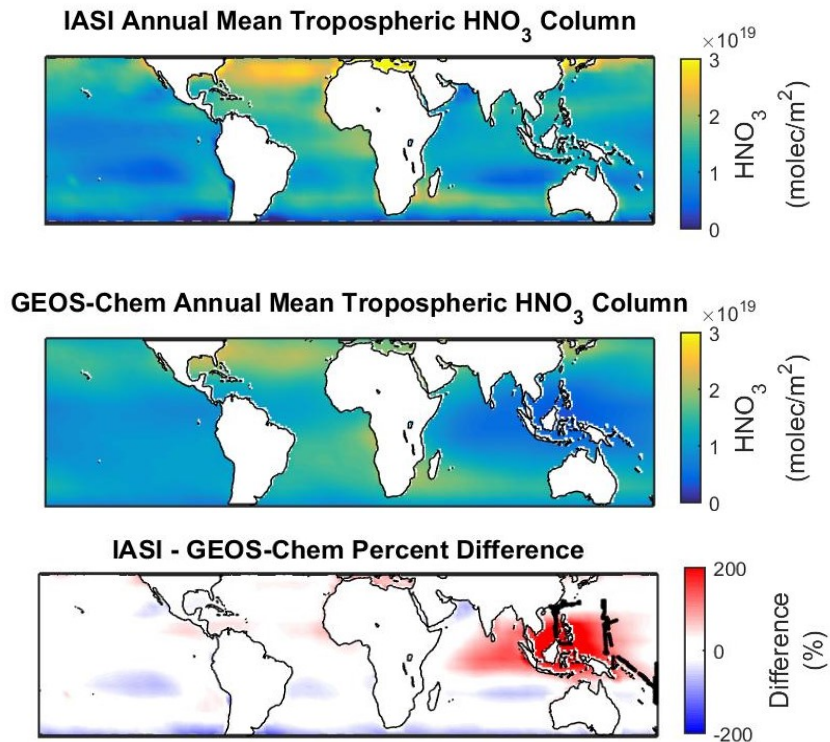
Figure 3-2: Annual mean tropospheric HNO$_3$ columns for 2008 from IASI (top) and GEOS-Chem (middle). The difference between IASI and GEOS-Chem is also shown (bottom). The location of PEMWest-B and PEM-Tropics A flight paths used here are shown in black in the bottom panel.

Figure 3-3 provides further evidence of a model bias through comparisons with additional satellite data. The far left panel of Figure 3-3 shows the relative deviation from the tropical mean tropospheric HNO$_3$ columns near the Equator (10°S-10°N) as a function of longitude for IASI and GEOS-Chem. The second panel shows this deviation calculated from the HIRDLS HNO$_3$ concentration at 163 hPa. The third panel uses ACE-FTS HNO$_3$ concentrations near 245 hPa. GEOS-Chem is sampled at the location and day of observations for each instrument. Since IASI gives column values and ACE-FTS and HIRDLS provide upper tropospheric concentrations, all three plots are normalized by their tropical mean values to facilitate comparisons, as well as to reduce the effect of instrument biases. All three plots show the familiar wave-one pattern of

elevated concentrations over the tropical Atlantic (longitude range 0°-20° and 310°-360°). IASI

shows a small local maximum over the Southeast Asia region (longitudes 60°-160°E) that is

more pronounced than that seen in the plots for ACE-FTS or HIRDLS. Differences between

instruments likely reflect different vertical layers of observation (column vs upper troposphere)

and sampling differences in this cloudy region. However, all three plots also show that GEOS-

Chem underestimates HNO_3 over this region. The ACE-FTS plot is consistent with previous

evaluations of GEOS-Chem by *Cooper et al.* [2011] that showed GEOS-Chem underestimates

NO_y concentrations relative to MOZAIC and HNO_3 relative to ACE-FTS in the region.
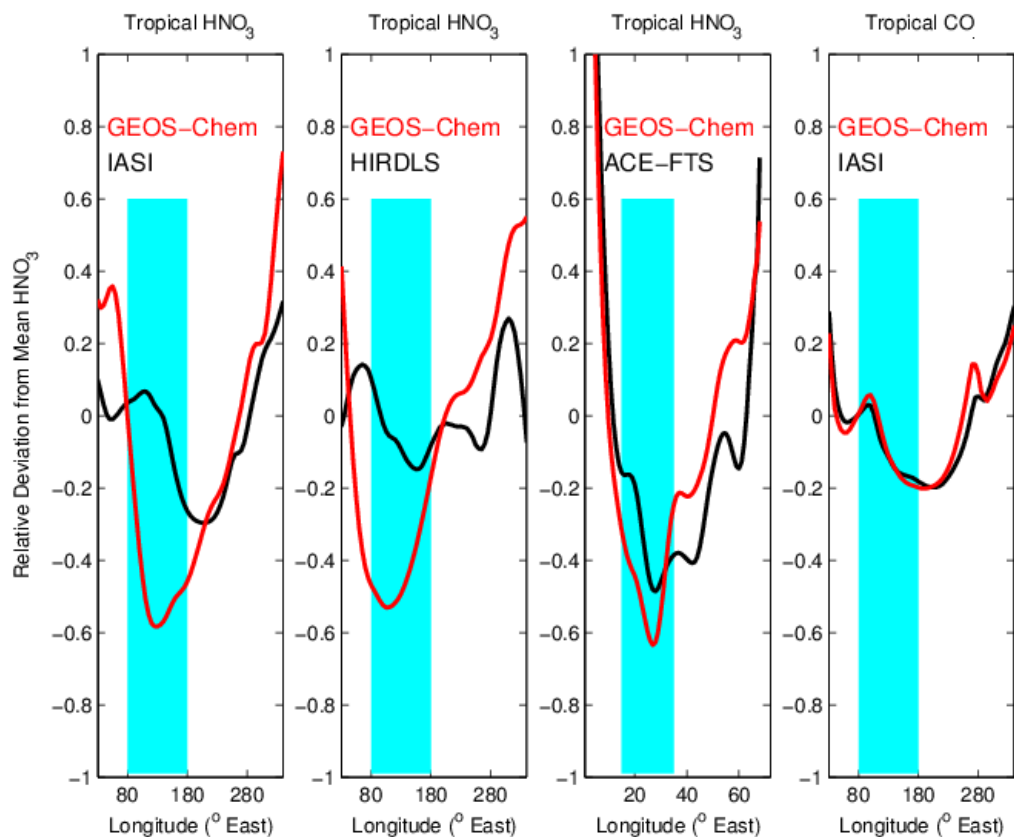
Figure 3-3: Relative deviation from tropical mean HNO₃ over 10S-10N. From left to right: GEOS-Chem and IASI HNO₃ tropospheric columns, GEOS-Chem and HIRDLS HNO₃ mixing ratios at 163 hPa, GEOS-Chem and ACE-FTS HNO₃ mixing ratios at 245 hPa, GEOS-Chem and IASI CO total columns. The first three panels show an underestimation in GEOS-Chem HNO₃ over Southeast Asia (shaded region spanning longitudes 80°-180°). The fourth panel shows no bias over Southeast Asia.

Figure 3-4 shows vertical HNO₃ profiles from measurements made in the Southeast Asia region only during the PEM-West B and PEM-Tropics A aircraft campaigns and from GEOS-Chem. The simulation is run using GMAO MERRA reanalysis meteorological fields for the campaign years (1994 for PEM-West B, 1996 for PEM-Tropics A) and is sampled along the aircraft flight path at the same location, altitude and time of the observations. The simulation is consistently lower than the aircraft measurements by a factor of 2-3 throughout the middle and

upper troposphere. This confirms the bias in the simulation, as this is a consistent feature over a large vertical and horizontal range observed independently by satellite and aircraft measurements.
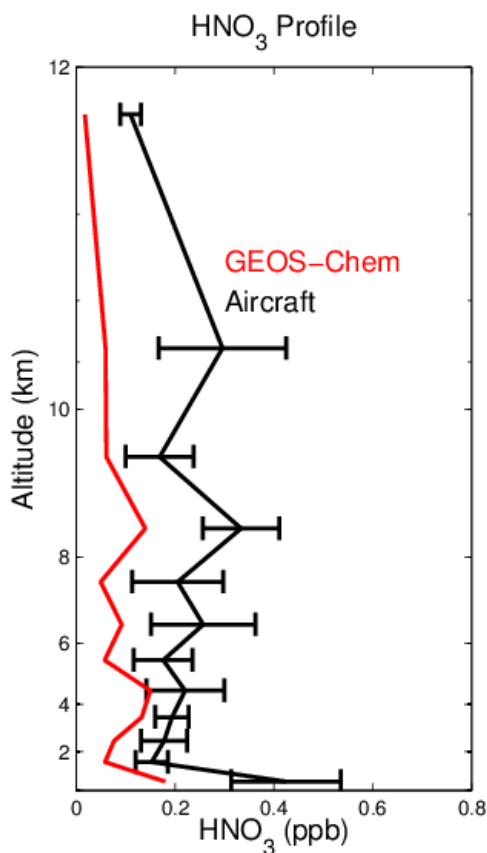
Figure 3-4: Average HNO₃ profiles from aircraft campaigns (PEM-West B and PEM-Tropics A) and from GEOS-Chem sampled along the flight paths. Error bars indicate one standard error from the mean.

3.6. Understanding the GEOS-Chem Bias

In the following sections we examine the most likely sources of the model underestimate in Southeast Asia: transport errors, the lightning NO_x source and its subsequent chemical processes, and overly vigorous wet deposition.

3.6.1 Mixing Processes

CO measurements are useful in model evaluation as combustion NO_x sources are collocated with CO emissions, and the lifetime of CO is sufficiently long to evaluate transport [*Jaeglé et al.,* 1998b]. The far right panel of Figure 3-3 shows the relative deviation from the tropical mean CO total columns for GEOS-Chem and IASI. The deviation from the mean in the GEOS-Chem simulation agrees well with IASI throughout the tropics, including the Southeast Asia region where the bias in HNO_3 exists. The absence of errors in CO indicates that transport from combustion sources is an unlikely contributor to the HNO_3 bias. We next turn to lightning NO_x as a potential contributor to the HNO_3 bias that is independent of CO.

3.6.2 Lightning NO_x Yield per Flash

We first examine the magnitude of the lightning NO_x source over Southeast Asia. In the year 2008 the standard GEOS-Chem simulation has a lightning NO_x source of 6.2 Tg N a^{-1}. Figure 3-5 shows the effect of adding additional lightning NO_x to the free troposphere. A factor of 3.5 increase in lightning NO_x yield/flash over Southeast Asia yields a 2.4 Tg N a^{-1} increase in the total global annual mean lightning NO_x source to 8.6 Tg N a^{-1}. The GEOS-Chem HNO_3 column bias versus IASI over the Indian Ocean and Indonesia is reduced from 92% to 7%. Agreement is also improved over the West Pacific. Figure 3-6 evaluates the implications for the O_3 simulation at Kuala Lumpur. The additional NO_x leads to increased ozone production which causes errors of 25% in the simulated ozone fields. This indicates that a simple increase in the lightning NO_x source is not the ideal solution to the simulated column HNO_3 underestimate.
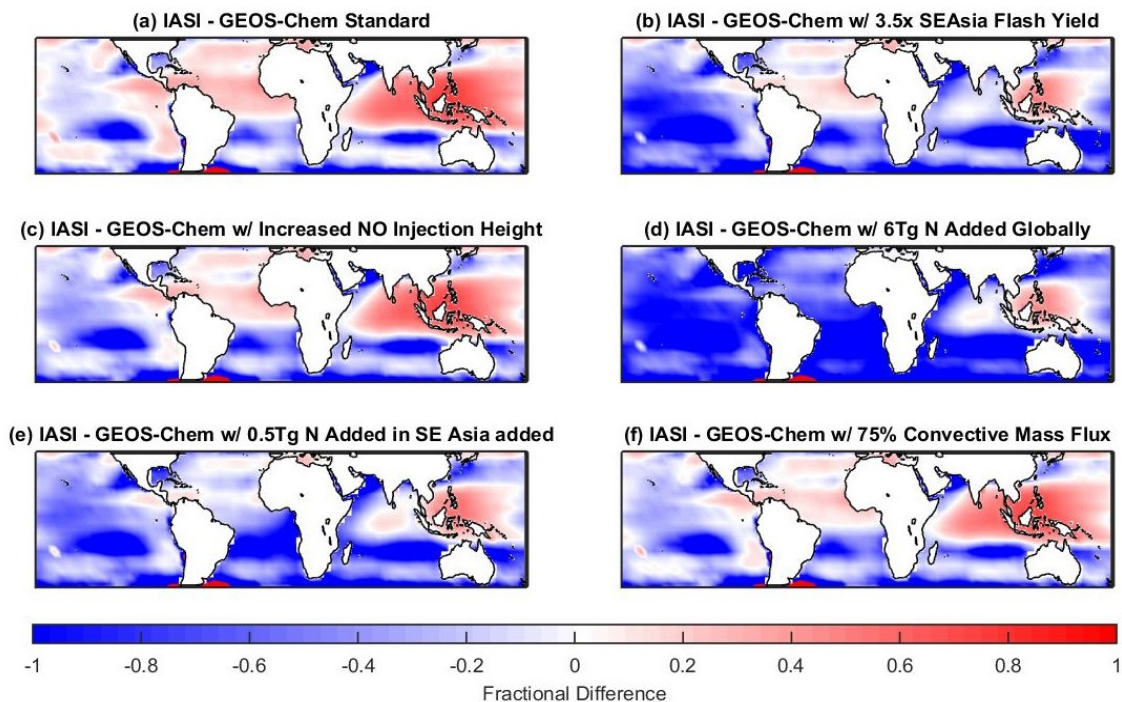
Figure 3-5: Fractional difference in annual mean tropospheric HNO_3 columns between IASI and the following GEOS-Chem simulations: (a) Standard simulation, (b) with flash yield increased by factor of 3.5 (c) with median NO injection height increased from 8.7 to 12.6 km (d) with 6 Tg additional HNO_3 globally, (e) with 0.5 Tg additional HNO_3 over Southeast Asia only, and (f) with convective mass fluxes reduced by 25%.

3.6.3 Vertical Distribution of Lightning NO_x

The effects of lightning NO_x on tropospheric chemistry depend on its vertical distribution, as NO_x lifetimes and ozone production efficiencies generally increase with altitude [*Labrador et al.,* 2005]. The profiles developed by *Ott et al.* [2010] used to distribute lightning NO_x emissions vertically are based on information from midlatitude and subtropical storms and might not be representative of tropical storms. We performed sensitivity studies by increasing the median injection height of tropical lightning NO emissions from 8.7 to 12.6 km. We find that raising the NO injection height increases the HNO_3 tropospheric column abundances throughout the tropics by as much as 25% but has little effect in the regions where lightning NO is emitted

as shown in Figure 3-5c. NO_x emitted at higher altitude has a longer lifetime and can be transported horizontally to form HNO_3 away from the source region. This HNO_3 also has a longer lifetime at these altitudes leading to the increased column abundances throughout the tropics. However near the region of emission the increase in HNO_3 produced at higher altitudes is largely balanced by decreases at lower altitudes and does not significantly change the column abundance. Thus adjustments to the NO_x injection height do not improve the simulation bias in Southeast Asia. The resulting change in ozone concentrations throughout the tropics is generally less than a few ppbv as shown in Figure 3-6.

3.6.4 Subgrid Plume Parameterization

The method by which lightning NO_x is emitted in the model may contribute to the model bias. Lightning NO_x emitted into the GEOS-Chem grid boxes produce dilute NO plumes with typical concentrations less than 1 ppbv. Aircraft observations found that lightning can create highly concentrated NO plumes inside cumulonimbus clouds, with concentrations generally between 1-7 ppbv and occasionally rising as high as 25 ppbv [*Huntrieser et al.*, 2002, 2009; *Ott et al.,* 2010]. These concentrated plumes can have spatial scales as small as 300 m [*Huntrieser et al.,* 2002] which are not resolved in global models with typical scales of 50-500 km. Ozone production from lightning NO_x is highly nonlinear with respect to NO_x concentration [*Lin et al.,* 1988]. As a result, the dilute NO_x plumes created in GEOS-Chem overestimate the ozone production efficiency (OPE), or the number of ozone molecules produced per NO_x molecule consumed. This means that O_3 is produced too efficiently and HNO_3 is produced too inefficiently. Similar issues have been noted in the representation of plumes from power plants [*Sillman et al.,* 1990], aircraft [*Meijer et al.,* 1997], and ships [*Vinken et al.,* 2011]. Changes to

39

the lightning NO_x parameterization which account for this nonlinearity may reduce the simulated

HNO_3 bias over Southeast Asia.
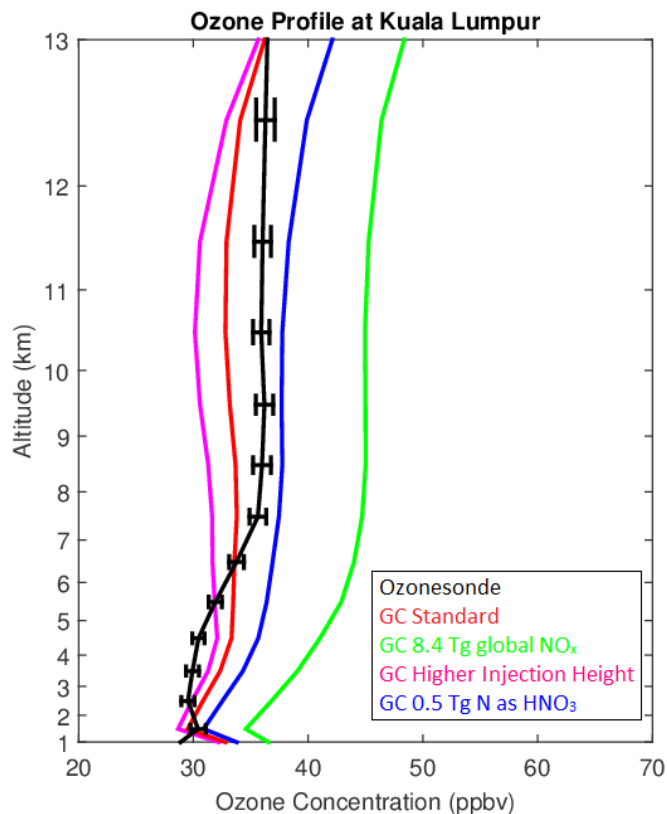
Figure 3-6: Annual mean ozone profile at Kuala Lumpur (2.7° N, 101.7° E). Profiles from a standard GEOS-Chem simulation (red), a simulation with 0.5 Tg HNO_3 added in Southeast Asia (blue), a simulation with the lightning NO source increased to 8.4 Tg (green), a simulation with lightning NO injection height raised to 12.6 km (pink), and an annual mean profile from ozonesondes (black) are shown. Error bars represent the standard error in the ozonesonde measurements.

We explored this process by modifying the GEOS-Chem lightning simulation to account

for the nonlinear chemistry that occurs in the early concentrated stage of a lightning NO_x plume

before it dilutes to grid box scale. This is done by allowing some of the lightning NO to rapidly

convert to HNO_3 after a typical amount of ozone production. The ratio of O_3 to HNO_3 produced

is treated as a constant OPE of 15 moles of O_3 per mole of HNO_3. This value was estimated by

forcing NO_x concentrations in a GEOS-Chem grid box over Indonesia to 5 ppbv (near the middle of the measured 1-7 ppbv range for lightning plumes), calculating the instantaneous OPE and finding an average of 15 moles O_3/mole NO. This value is similar to those found by modeling studies for urban pollution (5-20 mol/mol) [*Kleinman et al.,* 2002] and for aircraft NO_x emissions (10-28 mol/mol) [*Gilmore et al.,* 2013].

Figure 3-5d shows the change in HNO_3 from adding globally 6 Tg N yr^{-1} with an OPE of 15 mol/mol. The lightning NO source was held fixed at 6 Tg N a^{-1} while the amount of extra N (emitted as HNO_3) and O_3 was allowed to vary given uncertainty in plume dilution rates. The bias over Southeast Asia is reduced from 92% to 9%, but at the expense of increasing the bias throughout the rest of the tropics to -46%.

It is possible that lightning plumes over Southeast Asia have different behavior than elsewhere as lightning NO_x yields are known to vary by region [S*chumann and Huntrieser,* 2007]. Satellite observations show that lightning flashes in this region have higher radiances and have a larger spatial footprint than elsewhere in the tropics [*Beirle et al.,* 2014]. Also, intracloud lightning flashes, which dissipate more energy, occur more frequently in this region [*Corray* 1997; *Mackerras et al.,* 1998]. Lightning in GEOS-Chem is scaled by flash count and uses a single value for LNO_x produced per flash count in the tropics. Such parameterizations do not account for regional differences in flash radiance or length, or distinguish between intracloud and cloud-to-ground lightning, and are thus likely affected by regional biases. With this in mind, 0.5 Tg N is added with an OPE of 15 mol/mol over Southeast Asia only in Figure 3-5e. The bias over Southeast Asia is reduced to 6% without negatively affecting the rest of the tropics. Figure 3-6 evaluates how the additional O_3 (30 Tg) from this parameterization affects the O_3 simulation. Free tropospheric ozone concentrations in Southeast Asia increased by up to 7 ppbv (up to a 17%

increase) with small increases elsewhere. Ozone in the middle troposphere remains within 25% of ozonesondes at Kuala Lumpur.

3.6.5 Convection and Wet Deposition

The effects of convective activity on HNO_3 may play a role in the observed bias as Southeast Asia is a highly active convection region. *Staudt et al* [2003] found that simulated HNO_3 concentrations are sensitive to the convective mass flux due to both scavenging of HNO_3 in updrafts and mixing of air in the boundary layer where it can be deposited. We explored the potential effect that convection has on modeled HNO_3 by decreasing the convective mass flux by 25%. Figure 3-5f shows that this change in convective flux has little effect on the bias with respect to IASI tropospheric columns, increasing columns over the tropics by less than 15%. We also tested the effect of wet deposition alone, by reducing the scavenging efficiency in GEOS-Chem. A 50% reduction in the scavenging efficiency lead to a 10% increase in tropospheric HNO_3 columns. The reduction in solubility tested here is not physically likely, but these tests indicate that the convective scavenging scheme or errors in parameterized convection may play a role in the HNO_3 bias, although the overall sensitivity of the bias to scavenging is small compared to changes in lightning NO_x.

3.7 Conclusions

We analyzed IASI tropospheric HNO_3 columns over the tropical ocean. IASI and GEOS-Chem tropospheric HNO_3 columns are consistent within 10% throughout most of the tropics. However, observations over Southeast Asia show column values twice as high as simulated values. This simulated HNO_3 bias was confirmed by aircraft measurements (PEM-West B and PEM-Tropics A) and observations from the ACE-FTS and HIRDLS satellite instruments. Comparison of IASI and GEOS-Chem CO did not indicate a bias, implying large-scale transport errors are an unlikely explanation for the HNO_3 bias.

Investigation into the source of the model bias indicates sensitivity to the lightning NO_x parameterization. We found that direct changes to the lightning NO_x source was unlikely to explain the bias as a large (factor of 3.5) increase was needed, which in turn led to a 25% bias in simulated ozone concentrations relative to ozonesonde observations. Studies examining the sensitivity of tropospheric HNO_3 columns to the vertical distribution of lightning NO_x emissions showed that increasing the NO_x injection height had little effect on the simulation bias, although led to increased column abundances by 25% away from the region of emission. A simple parameterization accounting for nonlinearities in the conversion of NO_x to HNO_3 in the beginning stage of the lightning NO_x plume and the related ozone production chemistry was implemented with moderate success. A prescribed subgrid ozone production efficiency of 15 mol/mol in conjunction with an additional 0.5 Tg N added over Southeast Asia reduced the bias in that region from 92% to 6% with minimal impact on simulated ozone concentrations.

We also found some sensitivity of the model bias to convection processes, both in convective mass flux and the HNO_3 wet deposition parameterization. Improved agreement between IASI and GEOS-Chem in convectively active regions was achieved by either reducing the convective mass flux or the efficiency of wet scavenging in convective although the overall effects were small. The most likely solution to the model bias will include changes to multiple processes, although changes to lightning NO_x may have a greater effect.

Future work should consider a more sophisticated lightning plume model in which the OPE depends on local dilution rates, perhaps similar to the parameterization for ship emissions [*Vinken et al.,* 2011]. Additional processes not tested here, including errors in HNO_3 production from NO_2, HNO_3 photolysis in clouds, PAN chemistry, or uptake of HNO_3 by ice crystals [*von Kuhlmann and Lawrence,* 2006] may play a role. The recent development of a stratospheric

HNO$_3$ simulation for GEOS-Chem by *Eastham et al* [2014] will aid future efforts to separate stratospheric and tropospheric components from the IASI total columns.

3.8 Acknowledgements

Chapter 4: Comparing Mass Balance and Adjoint-Based 4D-Var Methods for Inverse Modeling of Nitrogen Dioxide Columns for Nitrogen Oxide Emissions

4.1 Abstract

Satellite observations offer information that can be applied for top-down constraints on emission inventories through inverse modeling. Here we compare two methods of inverse modeling for emissions of nitrogen oxides (NO_x) from nitrogen dioxide (NO_2) columns. The GEOS-Chem chemical transport model and its adjoint are used for inverse modeling. We treat the adjoint-based four dimensional variational (4D-Var) modeling approach for estimating top-down emissions as a benchmark against which to evaluate variations on the mass balance method. We use synthetic NO_2 columns generated from known NO_x emissions to serve as "truth". We find that error in mass balance inversions can be reduced by factor of two by using an iterative process and using finite difference to calculate the local sensitivity of a change in NO_2 columns to a change in emissions. In a simplified case study to recover local emission perturbations, horizontal smearing effects due to NO_x transport were better resolved by the adjoint approach than by mass balance. For more complex emission changes that reflect real world scenarios, the iterative finite difference mass balance and adjoint methods produce similar top-down inventories when inverting hourly synthetic observations, both reducing the *a priori* error by factors of 3-4. Inversions of data sets that simulate satellite observations from low Earth and geostationary orbits also indicate that both the mass balance and adjoint inversions produce similar results, reducing *a priori* error by a factor of 3. As the iterative finite difference mass balance method provides similar accuracy as the adjoint method, it offers the ability to estimate top-down emissions using models that do not have an adjoint.

4.2 Introduction

　　Emissions of nitrogen oxides ($NO_x \equiv NO + NO_2$) have wide-ranging effects across the Earth system. Exposure to NO_2 is associated with increased mortality rates [*Burnett et al.*, 2004; *Jerrett et al.*, 2013; *Crouse et al.*, 2015]. NO_x catalyzes the production of tropospheric ozone, an important contributor to radiative forcing and atmospheric oxidation [*Lacis et al.*, 1990; *Thompson*, 1992]. NO_x oxidizes in the atmosphere to form aerosol nitrate with implications for climate [*Adams et al.*, 2001]. Deposition of atmospheric NO_x and its oxidation products to the surface leads to acidification of soils and provides nutrient delivery [*Zhang et al.*, 2012]. The main sources of NO_x emission into the troposphere include fossil fuel combustion, soil, biomass burning, and lightning. Emission inventories of these sources have significant uncertainty, as direct inference of emissions is impeded by sparse *in situ* measurements. Furthermore, traditional "bottom-up" emission inventories derived from fuel consumption and activity data can be outdated given timescales of years to produce. "Top-down" emission estimates derived from inverse modelling of satellite NO_2 columns offer information to evaluate and improve current emission inventories.

　　The challenge of using satellite measurements to provide top-down constraints on emissions inventories has been approached using a variety of techniques as recently reviewed by *Streets et al.* [2013] and *de Foy et al.* [2014]. These techniques include Kalman filters [*Napelenok et al.*, 2008; *Mijling and van der A*, 2012; *Miyazaki et al.*, 2012; *Mijling et al.*, 2013; *Ding et al.*, 2015], Gaussian analytical techniques [*Beirle et al.*, 2011; *Fioletov et al.*, 2011, 2015; *Valin et al.,* 2013; *de Foy et al.*, 2015; *McLinden et al.,* 2016], mass balance, and four-dimensional variational data assimilation. The latter two techniques are discussed below.

The mass balance method has been widely used for constraining NO_x emission inventories on many spatial scales, encompassing global [e.g. *Leue et al.*, 2001; *Martin et al.*, 2003], regional [e.g. *Wang et al.*, 2007; *Boersma et al.*, 2008b; *Zhao and Wang*, 2009; *Lin et al.*, 2010; *Russell et al.*, 2010; *Ghude et al.*, 2013; *Jena et al.*, 2015; *Kemball-Cook et al.*, 2015; *Zyrichidou et al.*, 2015] and local domains [e.g. *Li et al.*, 2010; *Lu and Streets,* 2012; *Prasad et al.*, 2012; *Duncan et al.*, 2013; *Hilboll et al.*, 2013]. Mass balance inversions have been used for timely updates to emission inventories by exploiting the near-real-time availability of satellite observations [e.g. *Lamsal et al.*, 2011]. The mass balance method has also been applied to provide information on specific emission source types, such as fossil fuel, biomass burning, or soil [e.g. *Jaeglé et al.*, 2005; *Lin*, 2012; *Vinken et al.*, 2014], as well as for other short-lived species including VOCs [*Palmer et al.*, 2001] and SO_2 [*Lee et al.*, 2011].

Several types of mass balance methods exist. The most commonly used basic mass balance methodology assumes a direct linear relationship between NO_2 columns and local emissions NO_x emissions [*Martin et al.*, 2003]. This approach exploits the short (hours to days) lifetime of NO_x that limits its transport. Transport of NO_x away from emission sources can lead to a smearing effect that introduces error in mass balance inversions [*Palmer et al.*, 2003]. Smearing effects can also occur from nonlocal NO_x sources through chemical feedbacks and reservoir species [*Turner et al.*, 2012]. Errors may also occur due to nonlinearities in NO_x-ozone chemistry. Changes in NO_x concentration affect its lifetime through changes in OH availability [*Lin et al.*, 1988], which complicates the direct linear relationship between NO_x emissions and NO_2 concentrations assumed in basic mass balance method. Variations on the basic mass balance methodology have been used to account for these sources of error. Smoothing kernels that account for the influence of emissions adjacent to the observed NO_2 column have been used to

47

account for possible transport errors [*Toenges-Schuller et al.*, 2006; *Boersma et al.*, 2008a; *Konovalov et al.*, 2006; *Zyrichidou et al.*, 2015], and scale factors that account for the sensitivity of NO_2 columns to changes in local NO_x emissions has been used to address nonlinear chemistry affects [*Walker et al.*, 2010; *Lamsal et al.*, 2011; *Vinken et al.*, 2014; *Zhang et al.*, 2015; *Verstraeten et al.,* 2015]. Iterative approaches have been proposed to address the smearing effects from transport of NO_2 and nonlinear chemistry [*Zhao and Wang*, 2009; *Ghude et al.*, 2013; *Jena at al.*, 2015]. An evaluation of these different mass balance methodologies is needed to identify their relative abilities to recover emission sources.

A more formal inversion method, known as four-dimensional variational (4D-Var) data assimilation, is used extensively in inverse modelling of various trace gases [*Elbern et al.*, 2000; *Henze et al.*, 2009; *Kopacz et al.*, 2009; *Jiang et al.*, 2011; *Wells et al.*, 2014; *Wang et al.*, 2012; *Jiang et al.*, 2015] including NO_2 [*Müller and Stavrakou*, 2005; *Stavrakou et al.*, 2008; *Zhang et al.*, 2008; *Kurokawa et al.*, 2009; *Stavrakou et al.*, 2013]. The adjoint-based 4D-Var method seeks to minimize a cost function that accounts for both the difference in simulated and observed NO_2 columns, as well as for the difference between *a priori* and optimized emissions. The adjoint method efficiently calculates the cost function gradient at each of several iterations of a steepest decent algorithm, and propagates information from the observations backwards in time to determine emission scaling factors that minimize the cost function. The adjoint method is more computationally demanding than the mass balance method, but more fully accounts for feedbacks from non-local sources of NO_2 and for nonlinearities in NO_x chemistry.

In this study we evaluate the accuracy of the mass balance and adjoint-based 4D-Var techniques by inverting synthetic observations created from known emission inventories. Section 4.3 outlines the inversion methods tested here and describes the GEOS-Chem model. Horizontal

smearing effects are evaluated in Section 4.4. Tests for recovering regional emission changes are

in Section 4.5.

4.3 Inverse Modeling Methodology
4.3.1 The Mass Balance Method
4.3.1.1 Basic Mass Balanced Method
     The basic mass balance method exploits the high NO_2/NO_x ratio in the boundary layer

and the short NO_x lifetime relative to horizontal transport timescales by assuming a direct

relationship α between top-down NO_x emissions E_t and observed NO_2 columns Ω_o:

$$E_t = \alpha\Omega_o \tag{4-1}$$

where the linear coefficient α (units of s^{-1}) accounts for the NO_x lifetime and the ratio of NO_x to

NO_2. A common approach to calculate α as introduced by *Martin et al.* [2003] is with a chemical

transport model as

$$\alpha = \left(\frac{E_a}{\Omega_a}\right) \tag{4-2}$$

where E_a is the *a priori* NO_x emission inventory and the NO_2 columns Ω_a are provided by the

GEOS-Chem model from that simulation.

4.3.1.2 Finite Difference Mass Balance Method
     Lamsal et al. [2011] extended the mass balance method to apply satellite observations for

timely updates to anthropogenic NO_x emission inventories. They introduced a unitless scaling

factor β that accounts for the sensitivity of changes in NO_2 columns to local changes in NO_x

emissions,

$$\frac{\Delta E}{E} = \beta\frac{\Delta\Omega}{\Omega} \tag{4-3}$$

with $\Delta\Omega$ representing the change in column abundances driven by the change in emissions ΔE. β

was calculated by perturbing surface NO_x emissions from fossil fuel combustion by a fixed

amount (10% used here). This scaling factor inferred through finite difference linearizes the simulated relation of NO_2 columns with NO_x emissions at the current model state. This linearization reduces errors from nonlinear NO_x-OH chemistry and can account for the relative contribution of a specific source of NO_x emissions (e.g. fossil fuel) to the NO_2 column.

We apply β here to determine top-down emissions by finite difference mass balance:

$$E_t = E_a \left(1 + \frac{\Omega_o - \Omega_a}{\Omega_a}\beta\right) \tag{4-4}$$

as derived in Appendix B1. β is also affected by the vertical sensitivity of the observing instrument, as noted by *Vinken et al.* [2014]. UV-Vis instruments are generally more sensitive to NO_2 at higher altitudes than near the surface, and therefore the change in observed columns is less sensitive to changes in emissions at the surface. This vertical gradient in sensitivity decreases $\Delta\Omega$ in Equation 4-3 and thus increases β.

In regions with negligible fossil fuel emissions or low NO_2 column abundances, the β calculation is a ratio of small numbers and may not be representative of the true atmosphere. We control for these cases by limiting β values to the range 0.1-10. These limits affect fewer than 1% of observations.

4.3.1.3 Iteration
An iterative method is also examined for both basic and finite difference mass balance. In the iterative method, the top-down emissions are used scale the fossil fuel *a priori* emissions before a subsequent simulation, and the process is repeated until the normalized mean error changes by less than 5%. The β term is recalculated after each iteration to account for changes in the sensitivity of NO_2 to the updated emissions. Iterating on β offers the prospect of better

representing the NO_x chemical regime at the observed NO_2 column concentrations instead of the *a priori* model state.

4.3.2 The Adjoint-Based 4D-Var Method

The adjoint-based 4D-Var method aims to minimize a cost function *J* defined as:

$$J = \frac{1}{2}\sum_{c \in \mho}(\Omega - \Omega_o)^T S^{-1}(\Omega - \Omega_o) + \frac{1}{2}\gamma_r(p - p_a)^T S_p^{-1}(p - p_a) \tag{4-5}$$

where $\mho$ is the domain, in both time and space, over which observations are available, Ω refers to the modeled column, Ω_o are the vertical columns derived from the observations, S is the error covariance matrix for the observations, p_a are the *a priori* emission scaling factors, p are the optimized emission scaling factors, S_p is the error covariance matrix of the scaling factors, and γ_r is a regularization parameter that allows weighting of the cost function towards observations or emissions. The first term in the cost function evaluates the simulation against the observations, and the second term, called the penalty term, evaluates the deviation from the *a priori* emissions.

Each adjoint inversion uses one week to allow the simulation to reach steady state, and then uses two weeks of observations for the inversion.

4.3.3 *A Posteriori* Emission Estimates
Top-down information can be combined with bottom-up inventories to create *a posteriori* emission estimates $\hat{E}$. For the adjoint method, this is accomplished by including the penalty term in the cost function. For the mass balance method, we use an analytical solution to minimizing the cost function, which can be expressed as:

$$\hat{E} = E_a + g(\Omega_o - kE_a) \tag{4-6}$$

where *g* is the gain matrix that describes the sensitivity of the inversion to the observations given the relative weighting of the observational (σ_e) and bottom-up uncertainties (σ_a):

$$g = \frac{h\sigma_a^2}{h^2\sigma_a^2 + \sigma_\varepsilon^2} \qquad (4\text{-}7)$$

and h is a matrix that relates NO_x emissions to observed NO_2 columns, defined as:

$$\Omega_o = kE \qquad (4\text{-}8)$$

Previous studies using the analytic solution have estimated **k** by calculating the Jacobian matrix

of the model [*Kopacz et al.,* 2009; *Berchet et al.*, 2013; *Turner et al.*, 2015]. We solve for h using

the mass balance relationships in Equations 4-1 and 4-4 for basic and finite mass balance

methods respectively. Derivations for h are in Appendix B2

4.3.4 The GEOS-Chem Model and its Adjoint

The GEOS-Chem chemical transport model version 8-02-01 (www.geos-chem.org) is

used to determine the *a priori* NO_x emissions and NO_2 columns, and the forward run for the

adjoint method. The simulation uses assimilated meteorological fields for the year 2005 from

NASA's Goddard Earth Observing System (GEOS-5). GEOS-Chem includes a detailed

simulation of HO_x-NO_x-VOC-O_3-aerosol chemistry [*Bey et al.*, 2001; *Park et al.*, 2004]. The

model version used here has 47 vertical levels up to 0.01 hPa and a horizontal resolution of

$4° \times 5°$. The transport time step is 30 minutes, and the chemical mass balance equations in the

troposphere are integrated every hour. A two week simulation at this resolution takes about 1

hour. Sensitivity tests were also conducted at $2° \times 2.5°$ resolution.

The global *a priori* fossil fuel NO_x emissions are given by the Emission Database for

Global Atmospheric Research (EDGAR) inventory [*Olivier et al.*, 2005] with regional

overwrites from EPA/NEI99 over North America, from EMEP over Europe, CAC for Canada,

BRAVO for Mexico [*Kuhns et al.*, 2005], and by the *Streets et al.* [2006] inventory over East

Asia. Biomass burning emissions are from GFED2 [*van der Werf et al.*, 2010]. The global

lightning NO$_x$ source strength is constrained using satellite observations of O$_3$ [*Martin et al.,*

2007] and scaled to match satellite observed flash frequencies as described by *Murray et al.*

[*2012*]. Soil NO$_x$ emissions are as described by *Wang et al.* [*1998*]. The top panel of Figure 4-1

shows the standard NO$_x$ emission inventory used in the GEOS-Chem simulation. NO$_x$ emissions

are enhanced over the industrialized regions in the northern hemisphere, particularly eastern

North America, Europe, and eastern Asia.
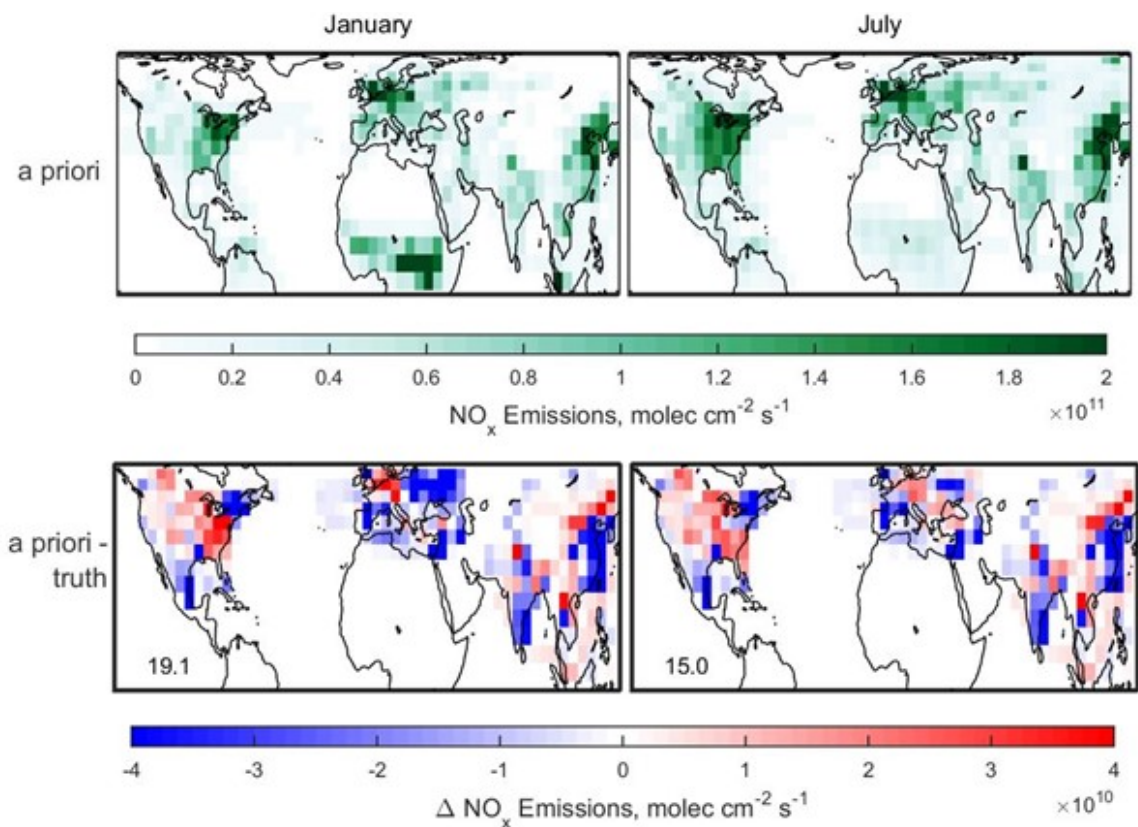
Figure 4-1: (Top) *a priori* NO$_x$ emissions. (Bottom) Difference between *a priori* NO$_x$ emissions
and the "truth" emissions used to create synthetic observations. "Truth" scenario was created by
using the EDGAR without the regional overwrites described in Chapter 4.3.4. Normalized mean
error (%) values are inset.

We used version 1.35 of the GEOS-Chem adjoint model. After the forward model is run,

the adjoint propagates information backward to calculate the cost function and adjoint forcings.

At the end of each iteration, the gradients are provided to the quasi-Newton L-BFGS-B optimization routine [*Byrd et al.*, 1995]. A full description of the adjoint can be found in *Henze et al.* [2007] with additional improvements described in *Henze et al.* [2009]. Each inversion took 20-30 iterations at about 2 hours per iteration at a 4°x5° horizontal resolution.

We conducted several sensitivity tests using synthetic observations so that a known "truth" can be used to evaluate the inversion methods. Normalized mean error values (NME) [*Boyland and Russell*, 2006] are used as a metric for evaluating emissions inventories against the truth.

4.3.5 Error Specification

The observational error is specified as $30\% + 1 \times 10^{15}$ molecules cm^{-2} for each observation. This error was selected to reflect the uncertainties in UV-Vis satellite observations, which are often specified as having an absolute component to the error that dominates away from sources and a relative component that dominates near sources [e.g. *Boersma et al.*, 2004; *Bucsela et al.*, 2013]. Higher assumed observational error leads to a larger influence from the *a priori* emissions. The *a priori* error in the fossil fuel emissions was specified as 50%.

4.4 Idealized Point Source Perturbations to Evaluate Smearing Effects

Errors in mass balance inversions due to smearing are evaluated by performing inversions on hourly synthetic observations produced by doubling fossil fuel emissions in four separate locations across the globe (Beijing, Johannesburg, London and Ohio). Figure 4-2 shows top-down results from mass balance and adjoint-based 4D-Var inversions using one week of synthetic observations. Significant smearing is apparent when using the basic mass balance method, particularly in the Northern Hemisphere in winter when reduced photochemistry leads to an increase in the NO$_x$ lifetime. The basic mass balance method exhibits an underestimation of NO$_x$ emissions in the perturbed source region and an overestimation in the adjacent areas

downwind. An iterative method greatly reduces these smearing effects, leading to a factor of 10 reduction in the inversion error in January after 9 iterations. Iteration allows the inversion to approach the "true" emissions at the location of perturbed source, and to reduce smearing downwind as the simulation propagates the effect of the emission change. The iterative finite difference mass balance further reduces the error by 30%. Figure 4-3 shows the error reduction as a function of iteration number. Fewer iterations are need in July as the smearing is less substantial. The adjoint-based 4D-Var inversion shows virtually no smearing and best retrieves the true emissions.

Table 4-1 summarizes the results from the horizontal smearing evaluations. A second test where emissions were perturbed by 30% in the same four locations showed consistent results. Table 4-1 also shows results of an additional test that was performed at 2°x2.5° horizontal resolution. Smearing is more pronounced at this finer resolution in January, with a factor of two higher error for the iterative finite difference mass balance, and a factor of 10 higher error for the adjoint method. Error values for July at finer resolution are slightly reduced for the mass balance methods, but a factor of 5 higher for the adjoint method. The increase in adjoint error at finer resolution is attributed to the increase in the number of degrees of freedom, which leads to a noisier solution to the adjoint. Although the iterative finite difference mass balance method greatly reduces error due to smearing, the adjoint-based 4D-Var inversion best retrieves the true emissions in this idealized scenario.
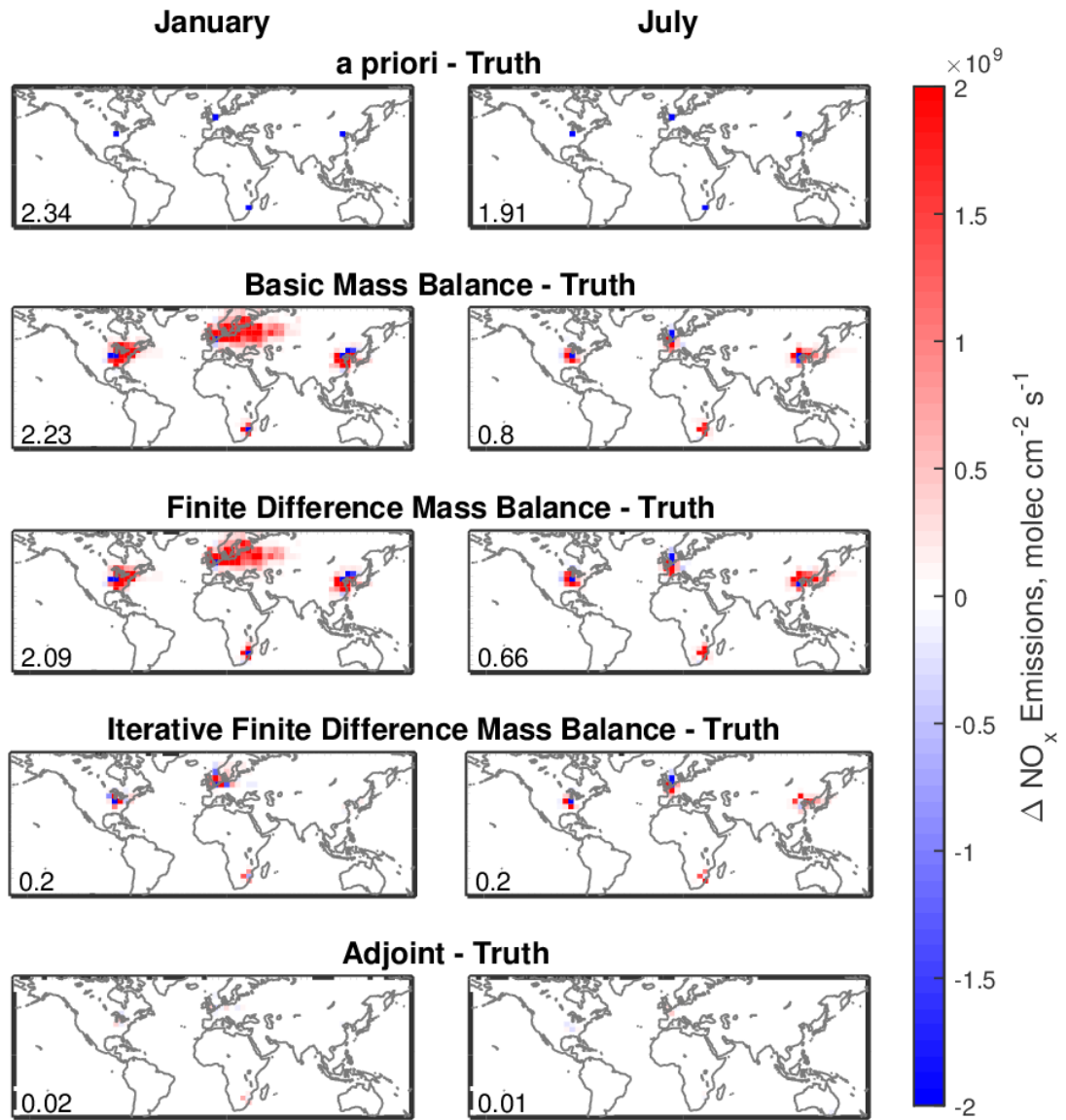
Figure 4-2: The top panel shows the difference between *a priori* NO$_x$ emissions and the "truth" emissions used to create synthetic observations for testing smearing effects. Other panels show inversion errors from mass balance and adjoint-based 4D-Var methods. Normalized mean error values (%) are inset.
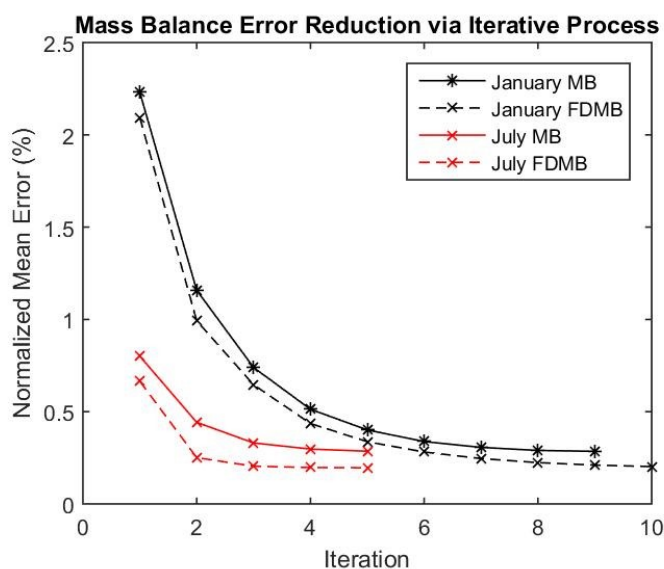
Figure 4-3: Normalized mean error reduction gained through an iterative method during the testing of horizontal smearing effects. Results using the basic mass balance (MB) and finite difference mass balance (FDMB) methods are shown.

Inversion Characteristics	Month	*a priori* NME (%)	Basic Mass Balance NME (%)	Iterative Finite Difference Mass Balance NME (%)	Adjoint NME (%)
Perturbed x 2, 4°x5° resolution	January	2.34	2.23	0.20	0.02
	July	1.91	0.80	0.20	0.01
Perturbed x 30%, 4°x5° resolution	January	0.71	0.62	0.08	0.02
	July	0.58	0.26	0.07	0.02
Perturbed x 2, 2°x2.5° resolution	January	2.45	2.89	0.44	0.29
	July	1.86	0.73	0.14	0.05

Table 4-1: Results from tests using idealized point source perturbations to evaluate smearing effects. Top-down inversions using the basic mass balance, iterative finite difference mass balance, and adjoint-based 4D-Var methods are shown. Normalized mean error (NME) represents the overall accuracy of each method.

4.5 Tests to Recover Heterogeneous Regional Emission Changes
4.5.1 Synthetic Observations

The bottom panel of Figure 4-1 shows a more complex and realistic distribution of emission errors. This "truth" scenario was created by using the standard fossil fuel emission inventory (EDGAR) without the regional overwrites described in Chapter 4.3.4. All non-fossil fuel emissions are unchanged. In this "truth" scenario, fossil fuel emissions are generally increased over eastern China, most of Europe, India, Mexico and the northeastern United States, and decreased over the eastern United States.

Synthetic observations of the "truth" scenario are made in four varieties:

1. Hourly observations

2. Observations with the spatial and temporal sampling of a Low Earth Orbit (LEO) satellite with morning overpass time (similar to the GOME2 instrument)

3. Observations with the spatial and temporal sampling of a LEO satellite with early afternoon overpass time (similar to the OMI instrument)

4. Hourly observations during daytime only, similar to the sampling of a geostationary satellite

For simulated LEO cases, the observations are sampled at the same spatial and temporal rate of the GOME2 and OMI instruments, and are smoothed to reflect their vertically-resolved instrument sensitivity. The cloud filtering algorithms of these instruments are also used to mimic real world sampling rates. No cloud filtering is performed for the simulated geostationary instruments.

4.5.2 Inversion Results

Figure 4-4 shows the difference between the true emissions and the top-down emission

estimates from all inversion methods for the standard synthetic observation scenario. Normalized mean errors are inset. The basic mass balance technique reduces the error from the *a priori* emissions by roughly a factor of two. The finite difference mass balance yields little improvement in January, as β values are near one, but has a significant impact in summer when non-fossil fuel emissions (biomass burning, soil, and lightning) make a larger contribution to the NO_2 column, reducing error by 40% over the basic mass balance method. Iterating the finite difference mass balance procedure further reduces the error, with a larger impact in January when horizontal smearing is more pronounced. For both months, the inversion with the lowest error is the iterative finite difference mass balance inversion, which reduces error by around a factor of two over the basic mass balance method. The adjoint-based 4D-Var inversion performs similarly to the iterative finite difference mass balance. The adjoint cost function reduces by an order of magnitude after 20-30 iterations.

The lower panels of Figure 4-4 show the results when top-down and bottom-up information are combined to form an *a posteriori* estimate. The iterative finite difference and adjoint methods produce similar *a posteriori* emission estimates. The penalty term in the adjoint cost function represents 20-30% of the total cost function value. The difference between the *a posteriori* and top-down estimates is small for both finite difference mass balance and adjoint inversions, as the *a priori* does not provide a strong constraint on the emissions.

Table 4-2 summarizes results from additional tests. Tests at a finer 2°x2.5° resolution yielded similar results in July, but larger errors in January due to more substantial smearing effects. Adding Gaussian random noise (σ = 30%) to the hourly synthetic observations similarly increased the error for both mass balance and adjoint inversions. For regions with β values larger than one, the finite difference mass balance amplifies the influence of the noise over the basic

mass balance, but overall the iterative finite difference mass balance still improves the inversion

over the basic mass balance.

Inversion Characteristics	Month	*a priori* NME (%)	Basic Mass Balance NME (%)	Iterative Finite Difference Mass Balance NME (%)	Adjoint NME (%)
(a) Inversions of synthetic observation					
Hourly Observations	January	19.1	10.1	5.7	6.5
	July	15.0	8.0	3.6	4.3
Synthetic LEO Morning	January	19.1	11.4	7.3	7.1
	July	15.0	8.5	5.1	5.3
Synthetic LEO Afternoon	January	19.1	9.7	5.7	7.7
	July	15.0	8.1	3.9	5.1
Synthetic Geostationary (Daytime only)	January	19.1	9.6	5.5	6.1
	July	15.0	7.3	4.6	4.1
(b) Resolution Effect test					
Hourly Observations, 4°x5° resolution	January	19.1	10.9	6.3	7.4
	July	15.0	8.2	3.5	4.3
Hourly Observations, 2°x2.5° resolution	January	22.2	14.6	11.5	14.4
	July	17.5	6.2	3.1	4.3
(c) Gaussian random noise or bias added to observations					
Hourly Observations, noise added	January	19.1	10.8	7.4	7.9
	July	15.0	8.5	4.5	5.1
Hourly Observations, noise and bias added	January	19.1	15.3	17.4	15.6
	July	15.0	12.4	13.6	13.8

Table 4-2: Results from inversions to recover heterogeneous regional emission changes using the basic mass balance, iterative finite difference mass balance, and adjoint-based 4D-Var methods for top-down estimates. Normalized mean error (NME) represents the overall accuracy of each method. Inversions are at 4°x5° horizontal resolution and an observational error of 30% + 1×10^{15} unless otherwise specified. Inversions are performed using two weeks of hourly observations in all cases except the synthetic LEO and geostationary cases in Section (a), which use the specified temporal sampling, and Section (b) which uses one week of observations for computational expediency at 2°x2.5°.

The optimal estimation framework used with the adjoint method treats observational

errors as random and unbiased. The mass balance method also assumes unbiased observations. In

practice UV-Vis satellite retrievals exhibit substantial unknown biases that arise in large part due

to errors in the treatment of geophysical fields such as surface reflectivity and clouds. To test the

effect of bias on the inversions, a bias was added to the observations in addition to the noise.

Bias values were assigned randomly to each grid box using a Gaussian distribution ($\sigma = 10\%$).

These results are summarized in Table 4-2. Biased observations increased the errors in the top-

down estimates from all inversion methods by 5-10 percentage points. *A posteriori* emission

estimates from biased observations have less error than the top-down estimates (NME reduced

by 1-3 percentage points), as the *a priori* constraint reduces the effect of bias in regions where

the *a priori* emissions are accurate. This constraint can be strengthened by increasing the

regularization parameter value to allow *a posteriori* emission estimates to be weighted closer to

the *a priori* estimate.
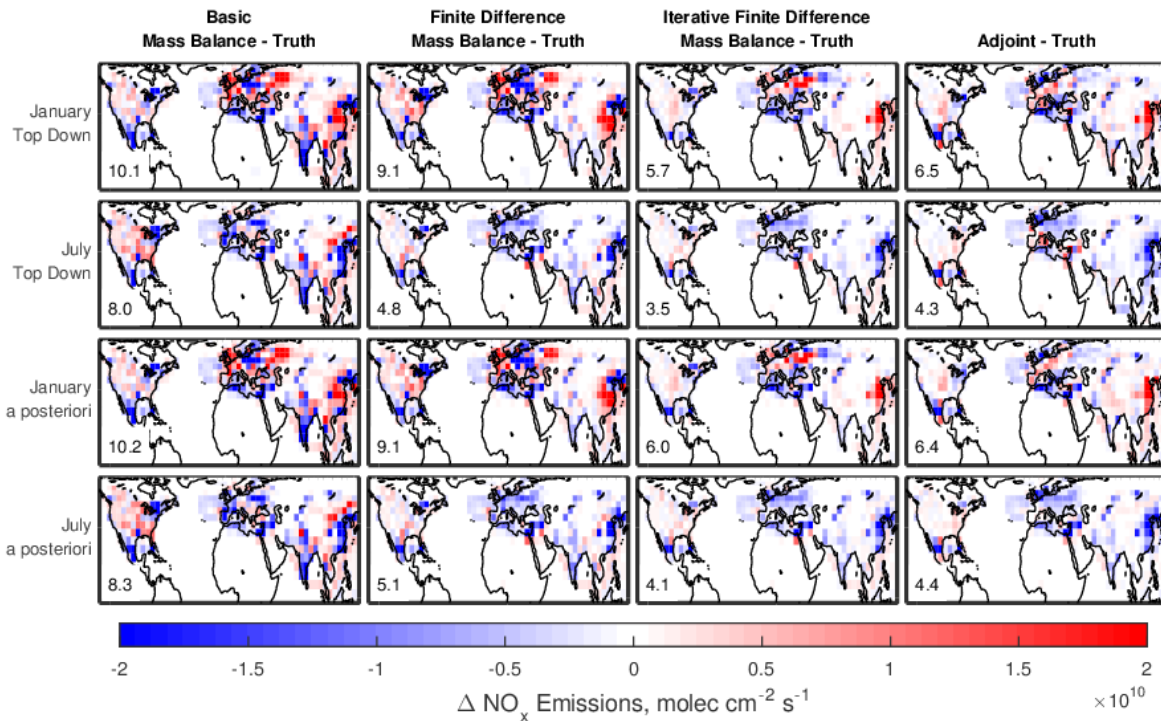
Figure 4-4: Comparisons between different inversion techniques and the known "truth"
emissions. Top-down refers to methods that are not weighted against *a priori* emissions. *a
posteriori* refers to emission estimates that combine top-down and *a priori* information.
Normalized mean error values (%) are inset.

Figure 4-5 shows results for inverting synthetic satellite observations. For the scenarios with synthetic LEO satellite observations, β values were calculated using NO_2 columns at the satellite overpass time and include the effects of vertically-resolved instrument sensitivity (scattering weights) of UV-Vis instruments. When using the basic mass balance method, all three synthetic satellite inversions perform similarly to the hourly base case with NME values ranging from 9.6-11.4% in January and 7.3-8.5% in July. Again, both the iterative finite difference mass balance and adjoint-based 4D-Var methods successfully reduce inversion error, achieving the lowest errors for the geostationary scenario, and the largest errors for the LEO morning scenario. The adjoint cost functions for the synthetic LEO and geostationary cases converged after 20-30 iterations, with the value of the cost function decreasing by 10-50% for LEO and by an order of magnitude for geostationary observations. The *a priori* term of the cost function represented 1-5% of the total cost function. The addition of noise to the synthetic observations led to a decrease in the relative contribution of the penalty term to the cost function compared to the noise-free hourly observation case. The greater density of forthcoming geostationary observations, and the finer spatial and temporal resolution that reduces bias from clouds and surface reflectivity, should offer stronger constraint on the NO_x emissions.
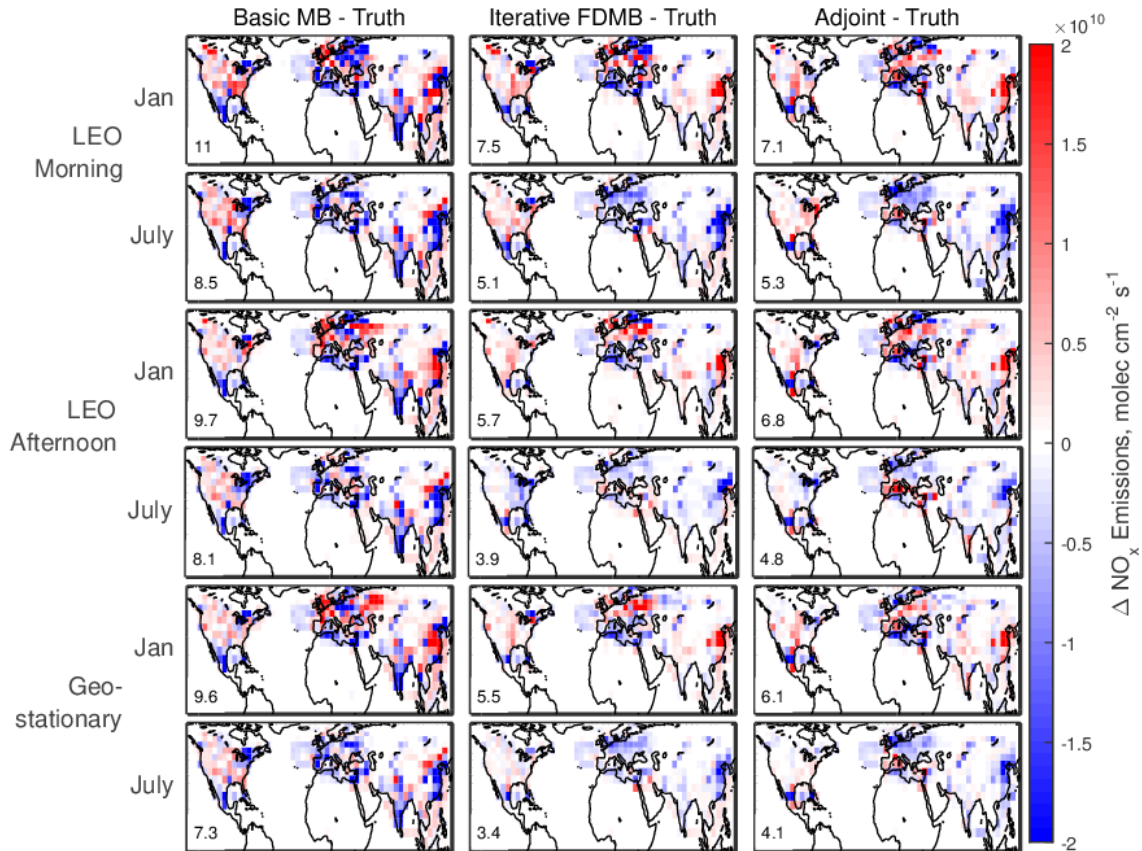
Figure 4-5: Inversion error for techniques using synthetic low Earth orbit (LEO) and geostationary satellite observations for basic mass balance (MB), iterative finite difference mass balance (FDMB), and adjoint methods. Normalized mean error values (%) are inset.

4.6 Conclusion

We present a comparison between two methods for inferring fossil fuel NO_x emissions from observed NO_2 columns. Synthetic observations generated from a chemical transport model (GEOS-Chem) are used to evaluate mass balance and adjoint-based 4D-Var inversion results, as they provide a known "truth" to measure inversion accuracy. We treat the adjoint-based 4D-Var method as a benchmark against which to assess the mass balance performance. Errors arise when using the basic mass balance method due to transport of NO_x and nonlinear NO_x-OH chemistry. We evaluate the ability of an iterative finite difference mass balance to reduce these errors by

linearizing the simulation about its *a priori* state and iterating until the model state approaches that represented by the observations.

To evaluate errors from horizontal smearing, a set of synthetic observations are constructed by perturbing emissions in four locations. Smearing effects are most prevalent in the northern hemisphere in January when the longer NO_x lifetime and stronger winds allow for more horizontal transport. These effects led to significant errors with the basic mass balance method that an iterative approach reduced by a factor of 10 in January. The adjoint-based 4D-Var inversion exhibited little smearing effects and best retrieved the true emissions in this case. This demonstrates an attribute of the adjoint method in terms of its ability to resolve the effects of complicated physical and chemical mechanisms.

A more realistic set of synthetic observations were created by using two different fossil fuel NO_x emission inventories across North America, Europe, and Asia. Inversions using hourly observations demonstrated that the iterative finite difference mass balance method improves upon the basic mass balance method. Iterating the mass balance procedure had a greater effect in January, as horizontal smearing is more prevalent in northern hemisphere winter. In July, the addition of the finite difference scaling factor has a larger impact, as it better identified the effects of fossil fuel combustion on NO_2 columns when other NO_x emissions make a larger contribution to the NO_2 column. Combining both of these modifications into an iterative finite difference mass balance method reduced the error from the basic mass balance method by a factor of two for both months. The iterative finite difference mass balance method yields top-down emission estimates that have errors as low as or lower than those achieved by the adjoint-based 4D-Var inversions. These results hold for both the 4°x5° and 2°x2.5° resolutions tested here.

The influence of noise and bias in observations was examined by imposing random noise and bias onto the synthetic observations. Observational noise leads to slight increases in error for both mass balance and adjoint-based 4D-Var inversions, but does not prevent either method from reducing the *a priori* error. Observational biases are not accounted for by either mass balance or adjoint methodologies, and thus lead to significant (greater than 50%) increases in inversion error. Incorporating knowledge from the *a priori* to form an *a posteriori* estimates reduced the effect of this bias.

Inversions using synthetic observations mimicking low Earth orbit and geostationary satellite observations were also tested. The accuracy of these inversions using the basic mass balance method was similar to that seen using hourly observations. Using an iterative finite difference method decreased errors in the mass balance method to a level comparable to the adjoint method. Both the iterative finite difference mass balance and adjoint methods benefitted from the greater density of geostationary observations.

In summary, an iterative finite difference mass balance inversion provides similar accuracy as the more rigorous adjoint-based 4D-Var method when estimating top down emissions inventories. Thus the finite difference mass balance offers the potential for top-down emission constraints using models that do not have an adjoint.

Chapter 5: Conclusions

5.1 Summary

Nitrogen oxides and ozone are involved in a wide variety of processes in the troposphere that affect air quality, atmospheric oxidation, and climate. NO_x is a catalyst in the production of tropospheric ozone. A strong understanding of the physical and chemical mechanisms that impact tropospheric NO_x and O_3 is therefore essential for both health and climate related research. This thesis presents results from three projects that show how satellite observations can be used in conjunction with a chemical transport model to enhance our understanding of how emissions, transport and chemistry affect the tropospheric NO_x-O_3 chemical system.

In Chapter 2, coherent spatial and temporal patterns of ozone concentrations less than 20 ppbv in the tropical upper troposphere are observed from space for the first time by the MLS, ACE-FTS, and OSIRIS satellite instruments. The frequency of low ozone events seen in the satellite record agreed with values in the ozonesonde record. These low ozone events occur most frequently in the convectively active region of the West Pacific warm pool, indicating a convective origin. The connection between low ozone events and active convection is strengthened by observed shifts in the frequency and location of low ozone events over the Pacific Ocean related to the El Niño-Southern Oscillation, with more frequent events over the central Pacific when the ocean beneath warms during El Niño conditions. Regions with frequent low ozone events are also observed to propagate eastward through the tropics with period and velocity typical to the Madden-Julian Oscillation.

Results from GEOS-Chem studies further support the hypothesis that the events result from deep convection, as the model was able to simulate the structure of the most frequent low ozone events only when convection is taken into account. The westward shift in low ozone event

frequency during La Niña was only partially resolved, indicating further developments to either the convective parameterization or assimilated meteorological fields are needed.

In Chapter 3, simulated HNO_3 columns over the tropical ocean were evaluated using observations from the IASI satellite instrument. GEOS-Chem tropospheric HNO_3 columns are consistent with IASI throughout most of the tropics, but are biased low by a factor of two over Southeast Asia. This simulated HNO_3 bias was confirmed by both aircraft measurements and observations from additional satellite instruments. Sensitivity studies concluded that the likeliest source of the model bias was the lightning NO_x parameterization. The diffuse lightning NO_x plumes simulated at the simulation's spatial resolution underestimates the conversion of NO_x to HNO_3 that occurs in the early, concentrated stage of the lightning NO_x plume. A simple parameterization accounting for conversion of NO_x to HNO_3 and the associated production of ozone in the beginning stage of the lightning NO_x plume was implemented with moderate success. A prescribed subgrid ozone production efficiency of 15 mol/mol in conjunction with an additional 0.5 Tg N added over Southeast Asia reduced the bias in that region from 92% to 6% with minimal impact on simulated ozone concentrations.

In Chapter 4, we examine mass balance and adjoint-based 4D-Var methods for inferring fossil fuel NO_x emissions from observed NO_2 columns. Synthetic observations generated from a chemical transport model (GEOS-Chem) are used to evaluate inversion results, as they provide a known "truth" to measure their accuracy. A case study with emissions perturbed in four separate locations is used as a test to evaluate these smearing effects. The basic mass balance method is prone to horizontal smearing errors due to transport of NO_x, particularly in January when the NO_x lifetime is longer. An iterative method was shown to reduce this error by a factor of 10 in

January, however the adjoint-based 4D-Var inversion showed little smearing effects and best retrieved the true emissions in this case.

Synthetic observations were created by perturbing fossil fuel NO_x emissions across North America, Europe, and Asia. Inversions using hourly observations demonstrated that the iterative finite difference method improves upon the basic mass balance method, reducing error by a factor of two. The iterative finite difference mass balance method yields top-down emission estimates that have a similar degree of error as the adjoint inversions. Inversions using synthetic observations mimicking low Earth orbit and geostationary satellite observations were also tested. The accuracy of these inversions using the basic mass balance method was similar to that seen using hourly observations.

Top-down information from the inversions was also combined with *a priori* information to form *a posteriori* emissions estimates. Using an *a posteriori* estimate of the error did not significantly change the inversion error, indicating that the *a priori* did not provide a strong constraint in this case.

5.2 Implications on Future Work

Convectively driven low ozone events demonstrate the important coupling between atmospheric dynamics and chemical composition. Ozone concentrations have been used in data assimilation analyses to gain useful information on thermodynamic processes [e.g. *Dee et al.*, 2011]. However, highly accurate measurements of composition are needed for these analyses, as poor measurement quality can have large influences on the results [*Peuch et al.*, 2000; *Miyazaki et al.,* 2014]. The strong relationship between convective activity and low ozone event frequency outlined in Chapter 2 indicates that low ozone event frequency, which is less strongly affected by

68

instrument biases than absolute concentration values, may be a useful tool in future data assimilation analyses. The link shown between low ozone events and convective oscillations, which can be observed without any frequency filtering, may be particularly useful for improving deficiencies in our understanding of the MJO that hamper both weather and climate forecasting [*Zhang*, 2013].

The work presented in Chapter 3 highlighted a deficiency that exists in GEOS-Chem and other chemical transport models regarding the parameterization of lightning NO_x. The recommendation at the conclusion of that work was that a more sophisticated lightning plume model would be beneficial to the modeling community. Since the publication of that study, a lightning plume model has been developed and implemented in GEOS-Chem [*Gressent et al.*, 2016]. The new plume-in-grid parameterization leads to decreases in NO_x, O_3, and HNO_3 in regions with lightning activity and subsequent increases upwind. *Gressent et al.* found a limited effect of NO_x conversion to HNO_3 in the plume, however the decrease in ozone production in the plume is consistent with the exploratory parameterization tested in Chapter 3.

Additional constraints on NO_x emissions continue to be needed to improve upon our understanding of air quality and climate issues. The work presented in Chapter 4 found that an iterative finite difference mass balance method is as effective a method for inverse modeling studies as the adjoint-based 4D-Var method. As it requires fewer computational resources, this demonstrates that the iterative finite difference mass balance is a nimble tool for future inverse modeling studies. Such work should take advantage of the earth observing instruments that are planned to launch on geostationary satellites overlooking North America (TEMPO), Europe (Sentinal-4) and East Asia (GEM) in the upcoming years. The iterative finite difference mass balance can take advantage of the greater density of observations from this next generation of

instruments and will provide useful information for further constraining NO_x emission inventories.

Appendix A: Author contributions

Chapters 2 and 3 contain articles that were published in *Geophysical Research Letters* and *Journal of Geophysical Research*. All text, figures, and results were contributed by the first author. In Chapter 2, these duties included calculating and mapping low ozone event frequencies for satellite datasets and ozonesondes, and determining relationships between event frequencies and ENSO and MJO. In Chapter 3, duties included scaling modeled stratospheric HNO_3 production and loss rates, determining tropospheric portion of the HNO_3 column, evaluating GEOS-Chem HNO_3 with satellite (IASI, HIRDLS, ACE-FTS) and aircraft observations, performing sensitivity studies to understand origin of the model underestimate, and developing the lightning NO_x pre-processor.

Randall Martin provided supervision and guidance during both projects. Other co-authors were members of teams responsible for production and validation of satellite data used in this project, and were consulted for insight into the data products and appropriate data usage. This includes Nathaniel Livesey (MLS O_3), Doug Degenstein (OSIRIS O_3), Kaley Walker (ACE-FTS O_3 and HNO_3), Catherine Wespes (IASI HNO_3), Pierre-Francois Coheur (IASI HNO_3), and Cathy Clerbaux (IASI CO). Lee Murray provided feedback on the lightning NO_x parameterization in GEOS-Chem and the pre-processors described in Chapter 3.

Appendix B: Derivations

B1. Finite Difference Mass Balance

We use finite difference to calculate the local relationship between surface NO_x emissions and NO_2 columns. One can estimate the top-down emissions E_t using a Taylor's series expansion of E_t around the *a priori* state of the model (Ω_a):

$$E_t = E_a + \left(\frac{\partial E}{\partial \Omega}\bigg|_{\Omega_a} \right) (\Omega_o - \Omega_a) + \cdots \tag{B1}$$

where E_a are the *a priori* emissions and Ω_a are the resulting simulated NO_2 columns. One can approximate the derivative using the beta scaling factor, which is calculated by perturbing the *a priori* emissions by 10% and calculating the resulting change in simulated column abundance.

$$\beta = \frac{\Delta E_a / E_a}{\Delta \Omega_a / \Omega_a} \tag{B2}$$

The derivative can thus be approximated by:

$$\frac{\partial E}{\partial \Omega}\bigg|_{\Omega_a} \approx \frac{\Delta E_a}{\Delta \Omega_a} = \beta \frac{E_a}{\Omega_a} \tag{B3}$$

Applying this approximation to Equation B1 and ignoring higher order terms gives the finite difference mass balance equation (Equation 4-4)

$$E_t = E_a + \beta \frac{E_a}{\Omega_a} (\Omega_o - \Omega_a) \tag{B4}$$

$$E_t = E_a \left(1 + \frac{\Omega_o - \Omega_a}{\Omega_a} \beta \right) \tag{B5}$$

B2. Analytic Solution to Minimize the Mass Balance Cost Function

To calculate an *a posteriori* emissions estimate, we use an analytic solution to minimizing the cost function using information from mass balance. We seek to find a linear relationship between NO_2 columns and NO_x emissions:

$$\Omega = hE \tag{B6}$$

If this relationship is known, then the analytical solution to minimizing the cost function can be given by:

$$\hat{E} = E_a + g(\Omega_o - hE_a) \tag{B7}$$

The coefficient h can be found using the mass balance equations. For basic mass balance (Equation 4-1), the solution is trivial:

$$E_t = \alpha\Omega_o = \frac{E_a}{\Omega_a}\Omega_o \tag{B8}$$

and therefore $h = \alpha^{-1} = \Omega_a/E_a$.

For finite difference mass balance, one can rearrange Equation 4-4 to show:

$$\Omega_o = \left(\frac{\Omega_a}{\beta E_a}\right)E_t + \Omega_a\left(\frac{\beta - 1}{\beta}\right) \tag{B9}$$

Here $h = \Omega_a/(\beta E_a)$, but unlike for the basic mass balance, using finite difference mass balance adds an offset to the linear relationship between Ω_o and E_t. The *a posteriori* emission estimate is then given by

$$\hat{E} = E_a + g\left(\Omega_o - \left(\frac{\Omega_a}{\beta E_a}\right)E_a - \Omega_a\left(\frac{\beta - 1}{\beta}\right)\right) \tag{B10}$$

References

Adams, P. J., Seinfeld, J. H., Koch, D., Mickley, L., and Jacob, D, (2001) General circulation model assessment of direct radiative forcing by the sulfate-nitrate-ammonium-water inorganic aerosol system, J. Geophys. Res., 106, 1097-1112.

Beirle, S., Boersma, K. F., Platt, U., Lawrence, M. G., and Wagner, T. (2011) Megacity Emissions and Lifetimes of Nitrogen Oxides Probed from Space, *Science*, 333, 1737-1739, 10.1126/science.1207824.

Beirle, S., W. Koshak, R. Blakeslee, and T. Wagner (2014), Global patterns of lightning properties derived by OTD and LIS, *Nat. Hazards Earth Syst. Sci. Discuss.* 2, 2765-2787, doi:10.5194/nhessd-2-2765-2014

Berchet, A et al. (2013) Towards better error statistics for atmospheric inversions of methane surface fluxes, *Atmos. Chem. Phys*., 13, 7115-7132, doi:10.5194/acp-13-7115-2013.

Bernath, P. F. et al. (2005), Atmospheric Chemistry Experiment (ACE): mission overview, *Geophys. Res. Lett.*, 32, L15S01, doi:10.1029/2005GL022386.

Bernath, P. F. (2006), Atmospheric Chemistry Experiment: Analytical chemistry from orbit, *Trends Analyt. Chem.*, 25, 647–654, doi:10.1016/j.trac.2006.05.001.

Bey, I., D. J. Jacob, R. M. Yantosca, J. A. Logan, B. Field, A. M. Fiore, Q. Li, H. Liu, L. J. Mickley, and M. Schultz (2001), Global modeling of tropospheric chemistry with assimilated meteorology: Model description and evaluation, *J. Geophys. Res.,* 106, 23,073-23,096.

Boersma, K.F., H.J. Eskes and E.J. Brinksma (2004), Error Analysis for Tropospheric NO_2 Retrieval from Space, *J. Geophys. Res*. 109 D04311, doi:10.1029/2003JD003962.

Boersma, K.F., H.J. Eskes, J.P. Veefkind, E.J. Brinksma, R.J. van der A, M. Sneep, G.H.J. van den Oord, P.F. Levelt, P. Stammes, J.F. Gleason and E.J. Bucsela (2007), Near-real time retrieval of tropospheric NO2 from OMI, *Atm. Chem. Phys*., 2013-2128, sref:1680-7324/acp/2007-7-2103.

Boersma, K. F., Jacob, D. J., Bucsela, E. J., Perring, A. E., Dirksen, R., van der A, R. J., Yantosca, R. M., Park, R. J., Wenig, M. O., Bertram, T. H., and Cohen, R. C. (2008a) Validation of OMI tropospheric NO2 observations during INTEX-B and application to constrain NOx emissions over the eastern United States and Mexico, *Atmos. Environ*., 42, 4480-4497, doi:4410.1016/j.atmosenv.2008.4402.4004.

Boersma, K. F., Jacob, D. J., Eskes, H. J., Pinder, R. W., Wang, J., and van der A, R. J. (2008b) Intercomparison of SCIAMACHY and OMI tropospheric NO2 columns: observing the diurnal evolution of chemistry and emissions from space, *J. Geophys. Res*., 113, D16S26, doi:10.1029/2007JD008816.

Boone, C.D., R. Nasser, K.A. Walker, Y. Rochon, S.D. McLeod, C.P. Rinsland, and P.F. Bernath (2005), Retrievals for the atmospheric chemistry experiment Fourier-transform spectrometer, *Applied Optics*, 44, 33, 7218-7231.

Boylan, J. W., and Russell, A. G. (2006) PM and light extinction model performance metrics, goals, and criteria for three-dimensional air quality models, *Atmos. Environ*., 40, 4946-4959, http://dx.doi.org/10.1016/j.atmosenv.2005.09.087.

Borucki W and Chameides, W (1984), Lightning: Estimate of the Rates of Energy Dissipation and Nitrogen Fixation, *Review of Geophysics and Space Physics* 22(4): 363:372.

Bucsela, E. J., Krotkov, N. A., Celarier, E. A., Lamsal, L. N., Swartz, W. H., Bhartia, P. K., Boersma, K. F., Veefkind, J. P., Gleason, J. F., and Pickering, K. E. (2013) A new stratospheric and tropospheric NO2 retrieval algorithm for nadir-viewing satellite instruments: applications to OMI, *Atmos. Meas. Tech*., 6, 2607-2626, 10.5194/amt-6-2607-2013.

Burnett, R. T., Stieb, D., Brook, J. R., Cakmak, S., Dales, R., and Raizenne, M. (2004), Associations between short-term changes in nitrogen dioxide and mortality in Canadian cities, *Arch. Environ. Health*, 59.

Brunner, D., Staehelin, J., Rogers, H. L., Köhler, M. O., Pyle, J. A., Hauglustaine, D. A., Jourdain, L., Berntsen, T. K., Gauss, M., Isaksen, I. S. A., Meijer, E., van Velthoven, P., Pitari, G., Mancini, E., Grewe, V., and Sausen, R. (2005) An evaluation of the performance of chemistry transport models - Part 2: Detailed comparison with two selected campaigns, *Atmos. Chem. Phys.*, 5, 107-129, doi:10.5194/acp-5-107-2005.

Byrd, R. H., Lu, P. H., Nocedal, J., and Zhu, C. Y. (1995) A Limited Memory Algorithm for Bound Constrained Optimization, *SIAM Journal on Scientific Computing*, 16, 1190-1208, doi: 1110.1137/0916069.

Chae, J.H., D.L. Wu, W.G. Read, and S.C. Sherwood (2011), The role of tropical deep convective clouds on temperature, water vapor, and dehydration in the tropical tropopause layer (TTL), *Atm. Chem. Phys.*, 11, 3811-3821.

Chandra, S., J. R. Ziemke, P. K. Bhartia, and R. V. Martin (2002), Tropical tropospheric ozone: Implications for dynamics and biomass burning, *J. Geophys., Res.*, 107, doi:10.129/2001JD000447

Chandra et al. (2003), Tropospheric ozone at tropical and middle latitudes derived from TOMS/MLS residual: Comparison with a global model, *J. Geophys. Res*., 108, doi: 10.1029/2002JD002912

Clerbaux, C. et al. (2009), Monitoring of atmospheric composition using the thermal infrared IASI/MetOp sounder, *Atm. Chem. Phys.* 9, 6041-6054.

Cooper, M., R.V. Martin, B. Sauvage, C.D. Boone, K.A. Walker, P.F. Bernath, C.A. McLinden, D.A. Degenstein, A. Volz-Thomas, and C. Wespes (2011), Evaluation of ACE-FTS and OSIRIS satellite retrievals of ozone and nitric acid in the tropical upper troposphere: Application to ozone production efficiency, *J. Geophys. Res.*, 116, D12306, doi:10.1029/2010JD015056.

Cooray, V. (1997), Energy dissipation in lightning flashes, *J. Geophysical Res.,* 102, D17, 21401-21410.

Crouse, D.L. et al. (2015) Within- and between-city contrasts in nitrogen dioxide and mortality in 10 Canadian cities; a subset of the Canadian Census Health and Environment Cohort (CanCHEC), *Journal of Exposure Science and Environmental Epidemiology* (2015) 25, 482–489; doi:10.1038/jes.2014.89.

Dee, D. P. et al., (2011), The ERA-Interim reanalysis: configuration and performance of the data assimilation system. *Q.J.R. Meteorol. Soc.*, 137: 553–597. doi:10.1002/qj.828

de Foy, B., Wilkins, J. L., Lu, Z., Streets, D. G., and Duncan, B. N. (2014) Model evaluation of methods for estimating surface emissions and chemical lifetimes from satellite data, *Atmos. Environ.*, 98, 66-77, http://dx.doi.org/10.1016/j.atmosenv.2014.08.051.

de Foy, B., Z. Lu, D.G. Streets, L.N. Lamsal, and B.N. Duncan (2015), Estimates of power plant NOx emissions and lifetimes from OMI NO2 satellite retrievals, *Atmos. Environ.*, 116, http://dx.doi.org/10.1016/j.atmosenv.2015.05.056 1352-2310

Ding, J., van der A, R. J., Mijling, B., Levelt, P. F., and Hao, N. (2015) NO_x emission estimates during the 2014 Youth Olympic Games in Nanjing, *Atmos. Chem. Phys.*, 15, 9399-9412, doi:10.5194/acp-15-9399-2015.

Duncan, B. N., Yoshida, Y., de Foy, B., Lamsal, L. N., Streets, D. G., Lu, Z., Pickering, K. E., and Krotkov, N. A. (2013) The observed response of Ozone Monitoring Instrument (OMI) NO2 columns to NOx emission controls on power plants in the United States: 2005–2011, *Atmos. Environ.*, 81, 102-111, http://dx.doi.org/10.1016/j.atmosenv.2013.08.068.

Degenstein, D. A., A. E. Bourassa, C. Z. Roth, and E. J. Llewellyn (2009), Limb scatter ozone retrieval from 10 to 60 km using a multiplicative algebraic reconstruction technique, *Atm. Chem. Phys.*, 9, 6521–6529, doi:10.5194/acp-9-6521-2009.

Eastham, S.D., D.K. Weisenstein, S.R.H. Barrett (2014), Development and evaluation of the unified tropospheric-stratospheric chemistry extension (UCX) for the global chemistry-transport model GEOS-Chem, *Atm. Environ.* 89, 52-63, doi:10.1016/j.atmosenv.2014.02.001

Elbern, H., Schmidt, H., Talagrand, O., and Ebel, A. (2000) 4D-variational data assimilation with an adjoint air quality model for emission analysis, *Environmental Modelling & Software*, 15, 539-548, http://dx.doi.org/10.1016/S1364-8152(00)00049-9.

Enfield, D.B (1989), El Nino, Past and Present, *Rev. Geophys.* 27, 1, 159-187.

EPA (2014), Policy Assessment for Ozone, EPA-452/R-14-006, EPA, Washington, DC, www.epa.gov/ttn/naaqs/standards/ozone/s_o3_index.html

Fioletov, V. E., McLinden, C. A., Krotkov, N., Moran, M. D., and Yang, K. (2011) Estimation of SO2 emissions using OMI retrievals, Geophys. Res. Lett., 38, L21811, 10.1029/2011gl049402.

Fioletov, V. E., C. A. McLinden, N. Krotkov, and C. Li (2015), Lifetimes and emissions of SO$_2$ from point sources estimated from OMI. *Geophys. Res. Lett.*, 42, 1969–1976. doi: 10.1002/2015GL063148.

Folkins, I., C. Braum, A. M. Thompson, and J. Witte (2002), Tropical ozone as an indicator of deep convection, *J. Geophys. Res.*, 107(D13), 4184, doi:10.1029/2001JD001178.

Folkins, I., P. Bernath, C. Boone, L. J. Donner, A. Eldering, G. Lesins, R. V. Martin, B.-M. Sinnhuber, and K. Walker (2006), Testing convective parameterizations with tropical measurements of HNO$_3$, CO, H$_2$O, and O$_3$: Implications for the water vapor budget, *J. Geophys. Res.*, 111, D23304, doi:10.1029/2006JD007325.

George, M., Clerbaux, C., Hurtmans, D., Turquety, S., Coheur, P.-F., Pommier, M., Hadji-Lazaro, J., Edwards, D. P., Worden, H., Luo, M., Rinsland, C., and McMillan, W.: Carbon monoxide distributions from the IASI/METOP mission: evaluation with other space-borne remote sensors, *Atmos. Chem. Phys.*, 9, 8317-8330, doi:10.5194/acp-9-8317-2009, 2009.

Ghude, S. D., Pfister, G. G., Jena, C., van der A, R. J., Emmons, L. K., and Kumar, R. (2013) Satellite constraints of nitrogen oxide (NOx) emissions from India based on OMI observations and WRF-Chem simulations, *Geophys. Res. Lett.*, 40, 423-428, 10.1002/grl.50065.

Gille, J.C. et al (1984), Accuracy and precision of the nitric acid concentration determined by the Limb Infrared Monitor of the Stratosphere experiment on the Nimbus 7, *J. Geophys. Res.,* 89, 5179-5190, doi:10.1029/JD089iD04p05179.

Gilmore, C.K., S.R.H. Barrett, J. Koo, and Q. Wang (2013), Temporal and spatial variability in the aviation NO$_x$-related O$_3$ impact, *Environ. Res. Lett.* 8, 034027, doi:10.1088/1748-9326/8/3/034027

Giorgi, F., and Chameides, W. L. (1986), Rainout lifetimes of highly soluble aerosols and gases as inferred from simulations with a general-circulation model, *J. Geophys. Res.*, 91, 14367-14376.

Granier, C. et al (2011), Evolution of anthropogenic and biomass burning emissions of air pollutants at global and regional scales during the 1980-2010 period, *Climate Change*, 109, 163-190.

Gressent, A., Sauvage, B., Cariolle, D., Evans, M., Leriche, M., Mari, C., and Thouret, V. (2016), Modeling lightning-NO$_x$ chemistry on a sub-grid scale in a global chemical transport model, *Atmos. Chem. Phys.*, 16, 5867-5889, doi:10.5194/acp-16-5867-2016.

Henze, D. K., Hakami, A., and Seinfeld, J. H. (2007) Development of the adjoint of GEOS-Chem, *Atmos. Chem. Phys.*, 7, 2413-2433.

Henze, D. K., Seinfeld, J. H., and Shindell, D. T. (2009) Inverse modeling and mapping U.S. air quality influences of inorganic PM2.5 precursor emissions with the adjoint of GEOS-Chem, *Atmos. Chem. Phys.*, 9, 5877-5903.

Hilboll, A., Richter, A., and Burrows, J. P. (2013) Long-term changes of tropospheric NO2 over megacities derived from multiple satellite instruments, *Atmos. Chem. Phys.*, 13, 4145-4169, 10.5194/acp-13-4145-2013.

Hoell, J. M., D. D. Davis, S. C. Liu, R. E. Newell, H. Akimoto, R. J. McNeal, and R. J. Bendura (1997),The Pacific Exploratory Mission-West Phase B: February-March, 1994, *J. Geophys. Res.*, 102(D23),28223–28239, doi:10.1029/97JD02581.

Hoell, J. M., D. D. Davis, D. J. Jacob, M. O. Rodgers, R. E. Newell, H. E. Fuelberg, R. J. McNeal, J. L. Raper, and R. J. Bendura (1999), Pacific Exploratory Mission in the tropical Pacific: PEM-Tropics A, August-September 1996, *J. Geophys. Res.*, 104(D5), 5567–5583, doi:10.1029/1998JD100074.

Hudman, R.C., N.E. Moore, A.k. Mebust, R.V. Martin, A.R. Russell, L.C. Valin, and R.C. Cohen (2012), Steps towards a mechanistic model of global soil nitric oxide emissions: implementation and space based constraints. *Atm. Chem. Phys.,* 12, 7779-7795, doi:10.5194/acp-12-7779-2012

Huntrieser, H., et al. (2002), Airborne measurements of NOx, tracer species, and small particles during the European Lightning Nitrogen Oxides Experiment, *J. Geophys. Res.*, 107(D11), doi:10.1029/2000JD000209.

Huntrieser, H., Schlager, H., Lichtenstern, M., Roiger, A., Stock, P., Minikin, A., Höller, H., Schmidt, K., Betz, H.-D., Allen, G., Viciani, S., Ulanovsky, A., Ravegnani, F., and Brunner, D. (2009) NO$_x$ production by lightning in Hector: first airborne measurements during SCOUT-O3/ACTIVE, *Atmos. Chem. Phys.*, 9, 8377-8412, doi:10.5194/acp-9-8377-2009.

Hurtmans, D., Coheur, P.-F., Wespes, C., Clarisse, L., Scharf, O., Clerbaux, C., Hadji-Lazaro, J., George, M., & Turquety, S. (2012). FORLI radiative transfer and retrieval code for IASI. *J. Quant. Spectro. & Rad. Transfer*, *113*(11), 1391-1408.

Jaeglé, L., Steinberger, L., Martin, R. V., and Chance, K. (2005) Global partitioning of NOx sources using satellite observations: Relative roles of fossil fuel combustion, biomass burning and soil emissions, *Faraday Discussions*, 130, 407-423, doi:410.1039/b502128f.

Jaeglé, L., D.J. Jacob, W.H. Brune, D. Tan, I.C. Faloona, A.J. Weinheimer, B.A. Ridley, T.L. Campos, G.W. Sachse (1998a), Sources of HO$_x$ and production of ozone in the upper troposphere over the United States, *Geophys. Res. Lett.* 25 (10) 1709-1712

Jaeglé, J., D.J. Jacob, Y. Wang, A.J. Weinheimer, B.A. Ridley, T.L. Campos, G.W. Sachse, D.E. Hagen (1998), Sources and chemistry of NOx in the upper troposphere over the United States, *Geophys. Res. Lett.* 25, 10, 1705-1708.

Jena,C., Ghude,S.D., Beig,G., Chate,D.M., Kumar,R., Pfister,G.G., Lal,D.M., Surendran,D.E., Fadnavis,S., and van der A,R.J. (2015) Inter-comparison of different NOX emission inventories and associated variation in simulated surface ozone in Indian region, *Atmospheric Environment*, 117, 61-73, ISSN 1352-2310, http://dx.doi.org/10.1016/j.atmosenv.2015.06.057.

Jerrett, M. et al. (2013), Spatial Analysis of Air Pollution and Mortality in California, American Journal of Respiratory and Critical Care Medicine, Vol. 188, No. 5, pp. 593-599, doi: 10.1164/rccm.201303-0609OC.

Jiang, Z., Jones, D. B. A., Worden, J., Worden, H. M., Henze, D. K., and Wang, Y. (2015) Regional data assimilation of multi-spectral MOPITT observations of CO over North America, *Atmos. Chem. Phys. Discuss*., 15, 5327-5358, doi:10.5194/acpd-15-5327-2015.

Jiang, Z., Jones, D. B. A., Kopacz, M., Liu, J., Henze, D. K., and Heald, C. (2011) Quantifying the impact of model errors on top-down estimates of carbon monoxide emissions using satellite observations, *Journal of Geophysical Research: Atmospheres*, 116, D15306, 10.1029/2010jd015282.

Johnson, J.E., R.H. Gammon, J. Larsen, T.S. Bates, S.J. Oltmans and J.C. Farmer (1990), Ozone in the marine boundary layer over the Pacific and Indian oceans: Latitudinal gradients and diurnal cycles, *J. Geophys. Res*, 95, D8, 11847-11856

Kasibhatla, P.S., H. Levey II and W.J. Moxim (1993), Global NO_x, HNO_3, PAN, and NO_y distributions from fossil fuel combustion emissions: A model study, *J. Geophys. Res.* 98 (D4) 7165-7180.

Kemball-Cook, S., Yarwood, G., Johnson,J., Dornblaser, B., Estes,M. (2015), Evaluating NOx emission inventories for regulatory air quality modeling using satellite and air quality model data, *Atmospheric Environment*, 117, 1-8, ISSN 1352-2310, http://dx.doi.org/10.1016/j.atmosenv.2015.07.002.

Kinnison, D.E. et al. (2008), Global observations of HNO_3 from the High Resolution Dynamics Limb Sounder (HIRDLS): First results, *J. Geophys. Res.* 113 (D16S44), doi:10.1029/2007JD008814.

Kleinman, L.I., P.H. Daum, Y-N Lee, L.J. Nunnermacker, S.R. Springston, J. Weinstein-Lloyd and J. Rudolph (2002), Ozone production efficiency in an urban area, *J. Geophys. Res.* 107 (D23), 4733, doi:10.1029/2002JD002529.

Kley, D., P.J. Crutzen, H.G.J. Smit, H. Vömel, S.J. Oltmans, H. Grassl, and V. Ramanathan (1996), Observations of near-zero ozone concentrations over the convective Pacific: Effects on air chemistry, *Science*, 274, 230-233, doi:10.1126/science.274.5285.230.

Konovalov, I. B., Beekmann, M., Richter, A., and Burrows, J. P. (2006) Inverse modelling of the spatial distribution of NOx emissions on a continental scale using satellite data, *Atmos. Chem. Phys.*, 6, 1747-1770.

Kopacz, M., Jacob, D. J., Henze, D. K., Heald, C. L., Streets, D. G., and Zhang, Q. (2009) Comparison of adjoint and analytical Bayesian inversion methods for constraining Asian sources of carbon monoxide using satellite (MOPITT) measurements of CO columns, *J. Geophys. Res.*, 114, D04305, doi: 04310.01029/02007JD009264.

Koshak, W. J., Peterson, H., Biazar, A., Khan, M., & Wang, L. (2013). The NASA Lightning Nitrogen Oxides Model (LNOM): Application to air quality modeling. *Atmospheric Research*. doi:10.1016/j.atmosres.2012.12.015

Kuhns, H., Knipping, E., and Vukovich, J. (2005) Development of a United States-Mexico Emissions Inventory for the Big Bend Regional Aerosol and Visibility Observational (BRAVO) Study, *J. Air Waste Manage. Assoc.*, 55, 677-692, doi: 610.1080/10473289.10472005.10464648.

Kurokawa, J.-i., Yumimoto, K., Uno, I., and Ohara, T. (2009) Adjoint inverse modeling of NOx emissions over eastern China using satellite observations of NO2 vertical column densities, *Atmos. Environ.*, 43, 1878-1887, http://dx.doi.org/10.1016/j.atmosenv.2008.12.030.

Labrador, L. J., von Kuhlmann, R., and Lawrence, M. G (2005), The effects of lightning-produced NO_x and its vertical distribution on atmospheric chemistry: sensitivity simulations with MATCH-MPIC, *Atmos. Chem. Phys.*, 5, 1815-1834, doi:10.5194/acp-5-1815-2005.

Lacis, A.A., D.J. Wuebbles and J.A. Logan (1990), Radiative forcing of climate by changes in the vertical distribution of ozone, *J. Geophys. Res.,* 95, 9971-9981, doi:10.1029/JD095iD07p009971

Lamsal, L. N., Martin, R. V., Padmanabhan, A., van Donkelaar, A., Zhang, Q., Sioris, C. E., Chance, K., Kurosu, T. P., and Newchurch, M. J. (2011) Application of satellite observations for timely updates to global anthropogenic NOx emission inventories, *Geophys. Res. Lett.*, 38, L05810, doi:05810.01029/02010GL046476.

Lawrence, M.G., R. von Kuhlmann, M. Salzmann and P.J. Rasch (2003), The balance of effects of deep convective mixing on tropospheric ozone, *Geophys. Res. Lett.* 30, 181940, doi:10.1029/2003GL017644

Lee, C., Martin, R. V., van Donkelaar, A., Lee, H., Dickerson, R. R., Hains, J. C., Krotkov, N., Richter, A., Vinnikov, K., and Schwab, J. J. (2011) SO2 emissions and lifetimes: Estimates from inverse modeling using in situ and global, space-based (SCIAMACHY and OMI) observations, *J. Geophys. Res.*, 116, D06304, doi:06310.01029/02010JD014758.

Lee, S., D.M. Shelow, A.M. Thompson, and S.K. Miller (2010), QBO and ENSO variablility in temperature and ozone from SHADOZ, 1998-2005, *J. Geophys. Res.* 115, D18105, doi:10.1029/2009JD013320

Leue, C., Wenig, M., Wagner, T., Klimm, O., Platt, U., and Jahne, B. (2001) Quantitative analysis of NOx emissions from GOME satellite image sequences, *J. Geophys. Res.*, 106, 5493-5505.

Li, C., Zhang, Q., Krotkov, N. A., Streets, D. G., He, K., Tsay, S.-C., and Gleason, J. F. (2010) Recent large reduction in sulfur dioxide emissions from Chinese power plants observed by the Ozone Monitoring Instrument, *Geophys. Res. Lett.*, 37, L08807, 10.1029/2010gl042594.

Lin, X., M. Trainer, and S.C. Liu (1988), On the nonlinearity of the tropospheric ozone production (1988), *J. Geophys. Res.,* 93 (D12), 15879-15888.

Lin, J.-T., McElroy, M., and Boersma, K. F. (2010) Constraint of anthropogenic NOx emissions in China from different sectors: A new methodology using multiple satellite retrievals, *Atmos. Chem. Phys.*, 10, 63-78.

Lin, J. T. (2012) Satellite constraint for emissions of nitrogen oxides from anthropogenic, lightning and soil sources over East China on a high- resolution grid, *Atmos. Chem. Phys.*, 12, 2881-2898, 10.5194/acp-12-2881-2012.

Liu, S. C., M. Trainer, F. C. Fehsenfeld, D. D. Parrish, E. J. Williams, D. W. Fahey, G. Huebler, and P. C. Murphy (1987), Ozone production in the rural troposphere and the implications for regional and global ozone distributions, *J. Geophys. Res.*, 92,4191–4207.

Liu, H., D.J. Jacob, I. Bey, and R.M. Yantosca (2001), Constraints from ^{210}Pb and [7]Be on wet deposition and transport in a global three-dimensional chemical tracer model driven by assimilated meteorological fields, *J. Geophys. Res.* 101 (D11) 12109-12128.

Livesey, N.J. et al (2011), EOS MLS Version 3.3 level 2 data quality and description document, Technical report, Jet Propulsion Laboratory, 18675-18677.

Livesey, N.J., J.A. Logan, M.L. Santee, J.W. Waters, R.M. Doherty, W.G. Read, L. Froidevaux, and J.H. Jiang (2012), Interrelated variations of O_3, CO and deep convection in the tropical/subtropical upper troposphere observed by the Aura Microwave Limb Sounder (MLS) during 2004-2011, *Atm. Chem. Phys.*, 13, 579-598, doi:10.5194/acp-13-579-2013.

Llewellyn, E. J., et al. (2004), The OSIRIS instrument on the Odin spacecraft, *Can. J. Phys.*, 82, 411–422.

Lu, Z., and Streets, D. G. (2012) Increase in NOx Emissions from Indian Thermal Power Plants during 1996–2010: Unit-Based Inventories and Multisatellite Observations, *Environ. Sci. Technol.*, 46, 7463-7470, 10.1021/es300831w.

Mackerras, D., M. Darveniza, R. E. Orville, E. R. Williams, and S. J. Goodman (1998), Global lightning: Total, cloud and ground flash estimates, *J. Geophys. Res.*, 103(D16), 19791–19809, doi:10.1029/98JD01461.

Madden, R.A. and P.R. Julian (1994), Observations of the 40-50 day tropical oscillation – A Review, *Mon. Weather Rev.*, 112, 814-837.

Mao, J. et al. (2010), Chemistry of hydrogen oxide radicals (HOx) in the Arctic troposphere in spring, *Atm. Chem. Phys.* 10(13), 5823-5838, doi: 10.5194/acp-10-5823-2010.

Mari, C. D.J. Jacob, and P. Bechtold (2000), Transport and scavenging of soluble gases in a deep convective cloud, *J. Geophys. Res.* 105(D17), 22255–22267, doi:10.1029/2000JD900211.

Martin, R.V., D.J. Jacob, J.A. Logan et al., (2002), Interpretation of TOMS observations of tropical tropospheric ozone with a global model and in situ observations, *J. Geophys. Res.* 107(D18),4351, doi:10.1029/2001JD001480.

Martin, R. V., Jacob, D. J., Chance, K., Kurosu, T. P., Palmer, P. I., and Evans, M. J. (2003) Global inventory of nitrogen oxide emissions constrained by space-based observations of NO2 columns, *J. Geophys. Res.*, 108, 4537, doi:4510.1029/2003JD003453.

Martin, R.V., B. Sauvage, I. Folkins, C.E. Sioris, C. Boone, P. Bernath, and J.R. Ziemke (2007), Space-based constraints on the production of nitric oxide by lightning, *J. Geophys. Res.*, 112, D09309, doi:10.1029/2006JD007831.

McLinden, C.A, S. C. Olsen, B. Hannegan, O. Wild, M. J. Prather, J. Sundet (2000), Stratospheric ozone in 3-D models: a simple chemistry and the cross-tropopause flux, *J. Geophys. Res.*, 105, 14653-14665.

McLinden, C.A., et al (2012), OSIRIS: A decade of scattered light, *Bull. Am. Meteo. Soc.* 93, 12, doi:10.1175/BAMS-D-11-00135.1

McLinden, C.A., V. Fioletov, M.W. Shephard, N. Krotkov, C. Li, R.V. Martin, M.D. Moran and J. Joiner (2016), Space-based detection of missing sulfur dioxide sources of global air pollution, *Nature Geoscience*, 9, 496-500, doi:10.1038/ngeo2724

Meijer, E.W., P.F.J. van Velthoven, W.M.F. Wauben, J.P. Beck, and G.J.M. Velders (1997), The effects of the conversion of nitrogen oxides in aircraft exhaust plumes in global models, *Geophys. Res. Lett.* 24, 23, 3013-3016

Mijling, B., and van der A, R. J. (2012), Using daily satellite observations to estimate emissions of short-lived air pollutants on a mesoscopic scale, *Journal of Geophysical Research: Atmospheres*, 117, D17302, 10.1029/2012jd017817.

Mijling, B., van der A, R. J., and Zhang, Q. (2013), Regional nitrogen oxides emission trends in East Asia observed from space, *Atmos. Chem. Phys.*, 13, 12003-12012, doi:10.5194/acp-13-12003-2013.

Mitovski, T., I. Folkins, R. V. Martin, and M. Cooper (2011), Testing convective transport on short timescales: comparisons with mass divergence and ozone anomaly patterns about high rain events, *J. Geophys. Res.*, 117, D02109, doi:10.1029/2011JD016321, 2012.

Miyazaki, K., Eskes, H. J., Sudo, K., Takigawa, M., van Weele, M., and Boersma, K. F. (2012) Simultaneous assimilation of satellite NO2, O3, CO, and HNO3 data for the analysis of tropospheric chemical composition and emissions, *Atmos. Chem. Phys.*, 12, 9545-9579, 10.5194/acp-12-9545-2012.

Miyazaki, K., H.J. Eskes, K. Sudo and C. Zhang (2014), Global lightning NO_x production estimated by an assimilation of multiple satellite data sets, *Atm. Chem. Phys.,* 14, 3277-3305, doi:10.5194/acp-14-3277-2014

Moorthi, S. and M. J. Suarez (1992), Relaxed Arakawa-Schubert, A Parameterization of Moist Convection for General-Circulation Models. *Mon. Wea. Rev.* 120, 978-1002.

Müller, J.-F., and Stavrakou, T. (2005), Inversion of CO and NOx emissions using the adjoint of the IMAGES model, *Atmos. Chem. Phys.*, 5, 1157-1186.

Murray, L. T., D. J. Jacob, J. A. Logan, R. C. Hudman, and W. J. Koshak (2012), Optimized regional and interannual variability of lightning in a global chemical transport model constrained by LIS/OTD satellite data, *J. Geophys. Res.*, 117, D20307, doi:10.1029/2012JD017934.

Murray, L.T., J.A. Logan, and D.J. Jacob (2013), Interannual variability in tropical tropospheric ozone and OH: the role of lightning, *J. Geophys. Res.*, doi: 10.1002/jgrd.50857

Napelenok, S. L., Pinder, R. W., Gilliland, A. B., and Martin, R. V. (2008) A method for evaluating spatially-resolved NOx emissions using Kalman filter inversion, direct sensitivities, and space-based NO2 observations, *Atmos. Chem. Phys.*, 8, 5603-5614.

Nassar, R., J. A. Logan, I. A. Megretskaia, L. T. Murray, L. Zhang, and D. B. A. Jones (2009), Analysis of tropical tropospheric ozone, carbon monoxide, and water vapor during the 2006 El Niño using TES observations and the GEOS-Chem model, *J. Geophys. Res.*, 114, D17304, doi:10.1029/2009JD011760.

Olivier J.G.J., et al. (2005), Recent trends in global greenhouse gas emissions: regional trends 1970-2000 and spatial distribution of key sources in 2000.*Env. Sc.*, 2(2-3), 81-99, doi: 918 10.1080/15693430500400345.

Oman, L.D., A.R. Douglass, J.R. Ziemke, J.M. Rodriguez, D.W. Waugh, and J.E. Nielsen (2013), the ozone response to ENSO in Aura satellite measurements and a chemistry-climate simulation, *J. Geophys. Res.,* 118, 1-12, doi:10.1029/2012JD018546.

Ott, L. E., K. E. Pickering, G. L. Stenchikov, D. J. Allen, A. J. DeCaria, B. Ridley, R.-F. Lin, S. Lang, andW.-K. Tao (2010), Production of lightning NO*x* and its vertical distribution calculated from three-dimensional cloud-scale chemical transport model simulations, *J. Geophys. Res.*, 115, D04301, doi:10.1029/2009JD011880.

Palmer, P. I., Jacob, D. J., Chance, K., Martin, R. V., Spurr, R. J. D., Kurosu, T. P., Bey, I., Yantosca, R., Fiore, A., and Li, Q. (2001), Air mass factor formulation for spectroscopic measurements from satellites: Application to formaldehyde retrievals from the Global Ozone Monitoring Experiment, *J. Geophys. Res.*, 106, 14539-14550.

Palmer, P. I., Jacob, D. J., Fiore, A. M., Martin, R. V., Chance, K., and Kurosu, T. P. (2003), Mapping isoprene emissions over North America using formaldehyde column observations from space, *J. Geophys. Res.*, 108, 4180, doi:4110.1029/2002JD002153.

Park, R. J., Jacob, D. J., Field, B. D., Yantosca, R. M., and Chin, M. (2004) Natural and transboundary pollution influences on sulfate-nitrate-ammonium aerosols in the United States: implications for policy, *J. Geophys. Res.*, 109, D15204, 15210.11029/12003JD004473.

Parrington, M et al (2012), The influence of boreal biomass burning emissions on the distribution of tropospheric ozone over North America and the North Atlantic during 2010, *Atm. Chem. Phys.* 12, 2077-2098, doi:10.5194/acp-12-2077-2012.

Peuch, A., Thépaut, J.-N. and Pailleux, J. (2000), Dynamical impact of total-ozone observations in a four-dimensional variational assimilation, *Q.J.R. Meteorol. Soc.*, 126: 1641–1659. doi:10.1002/qj.49712656605

Pickering, K. E., A. M. Thompson, R. R. Dickerson, W. T. Luke, D. P. McNamara, J. P. Greenberg, and P. R. Zimmerman (1990), Model calculations of tropospheric ozone production potential following observed convective events, *J. Geophys. Res.*, 95(D9), 14049–14062, doi:10.1029/JD095iD09p14049.

Prasad, A., Singh, R., and Kafatos, M. (2012) Influence of coal-based thermal power plants on the spatial–temporal variability of tropospheric NO_2 column over India, *Environ Monit Assess*, 184, 1891-1907, 10.1007/s10661-011-2087-6.

Rodgers, C.D. and B.J. Conner (2003), Intercomparison of remote sounding instruments, *J. Geophys. Res.* 108, D3, 4116, doi:10.1029/2002JD002299

Russell, A. R., Valin, L. C., Buscela, E. J., Wenig, M. O., and Cohen, R. C. (2010) Space-based constraints on spatial and temporal patterns of NOx emissions in California, 2005-2008, *Environ. Sci. & Tech.*, 44, 3608-3615.

Santee, M. L., G. L. Manney, N. J. Livesey, and W. G. Read (2004), Three-dimensional structure and evolution of stratospheric HNO_3 based on UARS Microwave Limb Sounder measurements, *J. Geophys. Res.*, 109, D15306, doi:10.1029/2004JD004578.

Sauvage, B., R. V. Martin, A. van Donkelaar, X. Liu, K. Chance, L. Jaeglé, P. I. Palmer, S. Wu, and T.-M. Fu (2007a), Remote sensed and in situ constraints on processes affecting tropical tropospheric ozone, *Atmos. Chem. Phys.*, 7, 815–838, doi:10.5194/acp-7-815-2007.

Sauvage, B., R. V. Martin, A. van Donkelaar, and J. R. Ziemke (2007b), Quantification of the factors controlling tropical tropospheric ozone and the South Atlantic maximum, *J. Geophys. Res.*, 112, D11309, doi:10.1029/2006JD008008.

Schumann, U. and H. Huntrieser (2007) The global lightning-induced nitrogen oxides source , *Atmos. Chem. Phys.*, 7, 3823-3907, doi:10.5194/acp-7-3823-2007

Sekiya, T. and K. Sudo (2012), Role of meteorological variablity in global tropospheric ozone during 1970-2008, *J. Geophys. Res.,* 117, D18303, doi: 10.1029/2012JD018054

Shiotani, M (1992), Annual, quasi-biennial, and El Nino-Southern Oscillation (ENSO) time-scale variations in equatorial total ozone, *J. Geophys. Res.*, 97, D7, 7625-7633.

Sillman, S., J. A. Logan, and S. C. Wofsy (1990), A regional scale model for ozone in the United States with subgrid representation of urban and power plant plumes, *J. Geophys. Res.*, 95(D5),5731–5748, doi:10.1029/JD095iD05p05731.

Singh, H. B., et al. (2007), Reactive nitrogen distribution and partitioning in the North American troposphere and lowermost stratosphere, *J. Geophys. Res.*, 112, D12S04, doi:10.1029/2006JD007664.

Solomon, S., D.W.J. Thompson, R.W. Portmann, S.J. Oltmans, and A.M. Thompson (2005), On the distribution and variability of ozone in the tropical upper troposphere: Implications for tropical deep convection and chemical-dynamical coupling, *Geophys. Res. Let.* 32, L23813, doi:10.1029/2005GL024323

Stavrakou, T., Müller, J. F., Boersma, K. F., De Smedt, I., and van der A, R. J. (2008) Assessing the distribution and growth rates of NOx emission sources by inverting a 10-year record of NO2 satellite columns, *Geophys. Res. Lett.*, 35, L10801, 10.1029/2008gl033521.

Staudt, A.C., D.J. Jacob, F. Ravetta, J.A. Logan, D. Bachiochi, T.N. Krishnamurti, S. Sandholm, B. Ridley, H.B. Singh, and B. Talbot (2003), Sources and chemistry of nitrogen oxides over the tropical Pacific, *J. Geophys. Res.,* 108, D2, 8239, doi:10.1029/2002JD002139

Stevenson, D. S., Young, P. J., Naik, V., Lamarque, J.-F., Shindell, D. T., Voulgarakis, A., Skeie, R. B., Dalsoren, S. B., Myhre, G., Berntsen, T. K., Folberth, G. A., Rumbold, S. T., Collins, W. J., MacKenzie, I. A., Doherty, R. M., Zeng, G., van Noije, T. P. C., Strunk, A., Bergmann, D., Cameron-Smith, P., Plummer, D. A., Strode, S. A., Horowitz, L., Lee, Y. H., Szopa, S., Sudo, K., Nagashima, T., Josse, B., Cionni, I., Righi, M., Eyring, V., Conley, A., Bowman, K. W., Wild, O., and Archibald, A. (2013), Tropospheric ozone changes, radiative forcing and attribution to emissions in the Atmospheric Chemistry and Climate Model Intercomparison Project (ACCMIP), *Atmos. Chem. Phys.*, 13, 3063-3085, doi:10.5194/acp-13-3063-2013.

Streets, D. G., Zhang, Q., Wang, L., He, K., Hao, J., Wu, Y., Tang, Y., and Carmichael, G. R. (2006), Revisiting China's CO emissions after the Transport and Chemical Evolution over the Pacific (TRACE-P) mission: Synthesis of inventories, atmospheric modeling, and observations, *J. Geophys. Res.*, 111, D14306, doi:14310.11029/12006JD007118.

Streets, D. G., Canty, T., Carmichael, G. R., de Foy, B., Dickerson, R. R., Duncan, B. N., Edwards, D. P., Haynes, J. A., Henze, D. K., Houyoux, M. R., Jacob, D. J., Krotkov, N. A., Lamsal, L. N., Liu, Y., Lu, Z., Martin, R. V., Pfister, G. G., Pinder, R. W., Salawitch, R. J., and Wecht, K. J. (2013) Emissions estimation from satellite retrievals: A review of current capability, *Atmos. Environ.*, 77, 1011-1042, http://dx.doi.org/10.1016/j.atmosenv.2013.05.051.

Thompson, A. M. (1992), The oxidizing capacity of the Earth's atmosphere: Probable past and future changes, *Science*, 256, 1157–1165, doi:10.1126/science.256.5060.1157.

Thompson, A. M., et al. (2003a), Southern Hemisphere Additional Ozonesondes (SHADOZ) 1998–2000 tropical ozone climatology: 1. Comparison with Total Ozone Mapping Spectrometer (TOMS) and ground-based measurements, *J. Geophys. Res.*, 108(D2), 8238, doi:10.1029/2001JD000967.

Thompson, A. M., et al. (2003b), Southern Hemisphere Additional Ozonesondes (SHADOZ) 1998–2000 tropical ozone climatology: 2. Tropospheric variability and the zonal wave-one, *J. Geophys. Res.*, 108(D2), 8241, doi:10.1029/2002JD002241.

Tian, B., Y.L. Yung, D.E. Waliser, T. Tyranowski, L. Kuai, E.J. Fetzer, and F.W. Irion (2007), Intraseasonal variations of the tropical total ozone and their connection to the Madden-Julian Oscillation, *Geophys. Res. Lett.* 34, L08704, doi: 10.1029/2007GL029451

Toenges-Schuller, N., Stein, O., Rohrer, F., Wahner, A., Richter, A., Burrows, J. P., Beirle, S., Wagner, T., Platt, U., and Elvidge, C. D. (2006) Global distribution pattern of anthropogenic nitrogen oxide emissions: Correlation analysis of satellite measurements and model calculations, *J. Geophys. Res.*, 111, D05312, doi:05310.01029/02005JD006068.

Tost, H., Joeckel, P. J., & Lelieveld, J. (2007). Lightning and convection parameterizations - uncertainties in global modelling. *Atmospheric Chemistry and Physics*, *7*(17), 4553–4568.

Tsidu, G.M., et al. (2005), NO_y from Michelson Interferometer for Passive Atmospheric Sounding on Environmental Satellite during the Southern Hemisphere polar vortex split in September/October 2002, *J. Geophys. Res.*, 110, D11301, doi:10.1029/2004JD005322.

Turner, A. J., Henze, D. K., Martin, R. V., and Hakami, A. (2012) The spatial extent of source influences on modeled column concentrations of short-lived species, *Geophys. Res. Lett.,* 39, L12806, 10.1029/2012gl051832.

Turner, A. J., et al., (2015). Estimating global and North American methane emissions with high spatial resolution using GOSAT satellite data. *Atmospheric Chemistry and Physics*, 15 (12), 7049-7069.

Valin, L. C., Russell, A. R., and Cohen, R. C. (2013), Variations of OH radical in an urban plume inferred from NO2 column measurements, *Geophys. Res. Lett.*, 40, 1856-1860, 10.1002/grl.50267.

van der Werf, G. R., Randerson, J. T., Giglio, L., Collatz, G. J., Mu, M., Kasibhatla, P. S., Morton, D. C., DeFries, R. S., Jin, Y., and van Leeuwen, T. T. (2010), Global fire emissions and the contribution of deforestation, savanna, forest, agricultural, and peat fires (1997–2009), *Atmos. Chem. Phys.*, 10, 11707-11735, doi:10.5194/acp-10-11707-2010

Verstraeten, W.W., Neu J.L., Williams, J.E., Bowman, K.W., Worden, J.R., and Boersma, K.F (2015), Rapid increases in tropospheric ozone production and export from China, *Nature Geoscience* 8, 690-695, doi:10.1038/ngeo2493

Vinken, G.C., K.F. Boersma, D.J. Jacob, and E.W. Meijer (2011), Accounting for non-linear chemistry of ship plumes in the GEOS-Chem global chemistry transport model, *Atm. Chem. Phys.,* 11, 11707-11722, doi:10.5194/acp-11-11707-2011.

Vinken, G. C. M., Boersma, K. F., Maasakkers, J. D., Adon, M., and Martin, R. V. (2014), Worldwide biogenic soil NOx emissions inferred from OMI NO2 observations, *Atmos. Chem. Phys.*, 14, 10363-10381, 10.5194/acp-14-10363-2014.

Von Kuhlmann, R. and M.G. Lawrence (2006), The impact of ice uptake of nitric acid on atmospheric chemistry, *Atm. Chem. Phys.,* 6, 225-235

von Savigny, C., I. C. McDade, E. Griffioen, C. S. Haley, C. E. Sioris, and E. J. Llewellyn (2005), Sensitivity studies and first validation of stratospheric ozone profile retrievals from Odin/OSIRIS observations of limb-scattered solar radiation, *Can. J. Phys.*, 83, 957–972.

Walker, T.W., R.V. Martin, A. van Donkelaar, W.R. Leaitch, A.M. Macdonald, K. Anlauf, R.C. Cohen, L.G. Huey, M.A. Avery, A.J. Weinheimer, F.M. Flocke, D.W. Tarasick, A.M. Thompson, D.G. Streets, and X. Liu (2010), Trans-Pacific transport of reactive nitrogen and ozone to Canada during spring, *Atmos. Chem. Phys.*, 10, 8353-8372.

Wang, J., Xu, X., Henze, D. K., Zeng, J., Ji, Q., Tsay, S.-C., and Huang, J. (2012), Top-down estimate of dust emissions through integration of MODIS and MISR aerosol retrievals with the GEOS-Chem adjoint model, *Geophys. Res. Lett.*, 39, L08802, 10.1029/2012gl051136.

Wang, Y. X., McElroy, M. B., Martin, R. V., Streets, D. G., Zhang, Q., and Fu, T.-M. (2007) Seasonal variability of NOx emissions over east China constrained by satellite observations: Implications for combustion and microbial sources, *J. Geophys. Res.*, 112, D06301, doi:06310.01029/02006JD007538.

Wang, Y., D.J. Jacob, and J.A. Logan (1998), Global Simulation of tropospheric O3-NOx-hydrocarbon chemistry: 1. Model formulation, *J. Geophys. Res.*, 103, pp. 10713-10725.

Wang, Q., D.J. Jacob, J.R Spackman, A.E. Perring, J.P. Schwarz, N. Moteki, E.A. Marais, C. Ge, J. Wang and S.R.H. Barrett (2013), Global budget and radiative forcing of black carbon aerosol: constraints from pole-to-pole (HIPPO) observations across the Pacific, *J. Geophys. Res.*, 2013JD020824, doi:10.1002/2013jd020824.

Wells, K. C., Millet, D. B., Cady-Pereira, K. E., Shephard, M. W., Henze, D. K., Bousserez, N., Apel, E. C., de Gouw, J., Warneke, C., and Singh, H. B. (2014) Quantifying global terrestrial methanol emissions using observations from the TES satellite sensor, *Atmos. Chem. Phys.*, 14, 2555-2570, doi:10.5194/acp-14-2555-2014.

Wespes, C. D. Hurtmans, C. Clerbaux, M.L. Santee, R.V. Martin and P.F. Coheur (2009), Global distributions of nitric acid from IASI/MetOP measurements, *Atm. Chem. Phys*. 9, 7949-7962.

Wolff, M. A., et al. (2008), Validation of HNO_3, $ClONO_2$, and N_2O_5 from the Atmospheric Chemistry Experiment Fourier Transform Spectrometer (ACE-FTS), *Atmos. Chem. Phys.*, 8, 3529–3562, doi:10.5194/acp-8-3529-2008.

Wong, S. and A.E. Dessler (2007), Regulation of H_2O and CO in tropical tropopause layer by the Madden-Julian Oscillation, *J. Geophys. Res.* 112, D14305, doi:10.1029/2006JD007940

Zhang, C. (2013) Madden–Julian Oscillation: Bridging weather and climate, *Bull. Amer. Meteor. Soc.*, 94, 1849–1870, doi: 10.1175/BAMS-D-12-00026.1

Zhang, L., Constantinescu, E. M., Sandu, A., Tang, Y., Chai, T., Carmichael, G. R., Byun, D., and Olaguer, E. (2008), An adjoint sensitivity analysis and 4D-Var data assimilation study of Texas air quality, *Atmos. Environ.*, 42, 5787-5804, http://dx.doi.org/10.1016/j.atmosenv.2008.03.048.

Zhang, L., D. J. Jacob, X. Liu, J. A. Logan, K. Chance, A. Eldering, and B. R. Bojkov (2010), Intercomparison methods for satellite measurements of atmospheric composition: Application to tropospheric ozone from TES and OMI, *Atmos. Chem. Phys. Discuss.*, 10, 1417–1456, doi:10.5194/acpd-10-1417-2010.

Zhang, L., Jacob, D. J., Knipping, E. M., Kumar, N., Munger, J. W., Carouge, C. C., van Donkelaar, A., Wang, Y. X., and Chen, D. (2012) Nitrogen deposition to the United States: distribution, sources, and processes, *Atmos. Chem. Phys.*, 12, 4539-4554, 10.5194/acp-12-4539-2012.

Zhang, Q. Q., Wang, Y., Ma, Q., Yao, Y., Xie, Y., and He, K. (2015), Regional differences in Chinese SO_2 emission control efficiency and policy implications, *Atmos. Chem. Phys.*, 15, 6521-6533, doi:10.5194/acp-15-6521-2015.

Zhao, C., and Wang, Y. (2009), Assimilated inversion of NOx emissions over East Asia using OMI NO2 column measurements, *Geophys. Res. Lett.*, 36, L06805, doi:06810.01029/02008GL037123.

Zhao, Y., Nielsen, C. P., Lei, Y., McElroy, M. B., and Hao, J. (2011) Quantifying the uncertainties of a bottom-up emission inventory of anthropogenic atmospheric pollutants in China, Atmos. Chem. Phys., 11, 2295-2308, doi:10.5194/acp-11-2295-2011.

Ziemke, J.R. and S. Chandra (2003), A Madden-Julian Oscillation in tropospheric ozone, *Geophys. Res. Lett.* 30, 2182, 4, doi:10.1029/2003GL018523.

Ziemke, J.R., S. Chandra, L.D. Oman, and P.K. Bhartia (2010), A new ENSO index derived from satellite measurements of column ozone, *Atm. Chem. Phys.*, 10, 3711-3721, doi:10.5194/acp-10-3711-2010.

Zyrichidou, I., M.E. Koukouli, D. Balis, K. Markakis, A. Poupkou, E. Katragkou, I. Kioutsioukis, D. Melas, K.F. Boersma, M. van Roozendael (2015), Identification of surface NOx emission sources on a regional scale using OMI NO2, *Atmospheric Environment*, 101, 82-93, ISSN 1352-2310, http://dx.doi.org/10.1016/j.atmosenv.2014.11.023.